

PAPER

Steady states of active Brownian particles interacting with boundaries

To cite this article: Caleb G Wagner et al J. Stat. Mech. (2022) 013208

View the article online for updates and enhancements.

You may also like

- Physics of microswimmers—single particle motion and collective behavior: a review J Elgeti, R G Winkler and G Gompper
- Static structure of active Brownian hard disks

N de Macedo Biniossek, H Löwen, Th Voigtmann et al.

 Predictive local field theory for interacting active Brownian spheres in two spatial dimensions

Jens Bickmann and Raphael Wittkowski



IOP ebooks™

Bringing together innovative digital publishing with leading authors from the global scientific community.

Start exploring the collection-download the first chapter of every title for free.

PAPER: Classical statistical mechanics, equilibrium and non-equilibrium

Steady states of active Brownian particles interacting with boundaries

Caleb G Wagner^{1,*}, Michael F Hagan² and Aparna Baskaran²

- Mechanical and Materials Engineering, University of Nebraska-Lincoln, Lincoln, NE 68588, United States of America
- ² Martin Fisher School of Physics, Brandeis University, Waltham, MA 02453, United States of America

E-mail:c.g.wagner
23@gmail.com, hagan@brandeis.edu and aparna@brandeis.edu

Received 5 September 2021 Accepted for publication 10 December 2021 Published 31 January 2022



Online at stacks.iop.org/JSTAT/2022/013208 https://doi.org/10.1088/1742-5468/ac42cf

Abstract. An active Brownian particle is a minimal model for a self-propelled colloid in a dissipative environment. Experiments and simulations show that, in the presence of boundaries and obstacles, active Brownian particle systems approach nontrivial nonequilibrium steady states with intriguing phenomenology, such as accumulation at boundaries, ratchet effects, and long-range depletion interactions. Nevertheless, theoretical analysis of these phenomena has proven difficult. Here, we address this theoretical challenge in the context of noninteracting particles in two dimensions, basing our analysis on the steady-state Smoluchowski equation for the one-particle distribution function. Our primary result is an approximation strategy that connects asymptotic solutions of the Smoluchowski equation to boundary conditions. We test this approximation against the exact analytic solution in a 2D planar geometry, as well as numerical solutions in circular and elliptic geometries. We find good agreement so long as the boundary conditions do not vary too rapidly with respect to the persistence length of particle trajectories. Our results are relevant for characterizing long-range flows and depletion interactions in such systems. In particular, our framework shows how such behaviors are connected to the breaking of detailed balance at the boundaries.

^{*}Author to whom any correspondence should be addressed.

Keywords: active matter

Contents

1. Introduction	2
2. Model definitions	4
3. Review of 1D problems	5
4. Method of solution for 2D problems	6
5. Benchmarking the framework: planar geometry	
5.1. Separation of variables	9
5.2. Diffusion solutions	9
5.3. Boundary layer solutions	
5.4. Full solution of a boundary value problem	
5.5. Validation of the diffusion approximation	13
6. Illustration 1: circular geometry	16
6.1. Problem statement	
6.2. Diffusion solution	
6.3. Symmetric circular geometry	
6.4. Asymmetric circular geometry	
7. Illustration 2: elliptic geometry	
7.1. Problem setup	
7.1. Troblem setup	
8. Summary	$\dots 25$
Acknowledgments	26
Appendix A. Numerical methods	26
Appendix B. Supplementary material for the 2D planar problem	28
•	
B.1. Completeness conjectures	
•	
Appendix C. Locally planar approximation	30
References	33

1. Introduction

Active matter describes a class of systems that are maintained far from equilibrium by driving forces acting on the constituent particles [1–10]. Experimental realizations span many scales, from the microscopic and colloidal to the macroscopic. Examples on the microscopic level are reconstituted biopolymers and molecular motors [11], bacterial suspensions [12, 13], and synthetic self-propelled colloids [14–16]. On larger scales, many macrobiological systems can be thought of as active matter, including swarming midges [17, 18], aggregating fire ants [19], schooling fish [20, 21], and flocking birds [22]. There are also examples of macroscopic active systems constructed artificially, such as vibrated self-propelled granular particles [23–28] and small robots [29–32].

At an abstract level, active matter is a promising testing bed for the development of new ideas about nonequilibrium steady states in general. It is already known that active matter steady states exhibit many unusual properties. Examples are the nonexistence of state variables like pressure and temperature [26, 33], violations of extensivity [34], aggregation at boundaries [35–39], and athermal phase separation [40–48]. Moreover, while equilibrium systems obey detailed balance and cannot exhibit net currents, this is no longer true out of equilibrium. Strikingly, in active matter systems, currents can occur even without external driving, instead resulting from rectification of the particle-level active driving by way of spatial asymmetries in the boundary conditions [49, 50].

At the concrete level, progress toward a fundamental understanding of these unusual phenomena requires minimal models that reproduce characteristically nonequilibrium phenomenology, while still being amenable to theoretical treatment. In this work, we focus on a simple, well-studied model for active matter, namely, a non-interacting collection of active Brownian particles (ABPs). This minimal model exhibits several of the features of nonequilibrium steady states mentioned above, including accumulation at boundaries, nonlocal probability measures, and long-ranged currents in steady-state. In particular, the existence of long-ranged currents was first shown by Baek et al [51], who derived a multipole expansion for the density and current exterior to a fixed, passive inclusion. These solutions do not require external forcing, in agreement with previous simulation results on active ratchet systems [50]. Instead, geometric constraints imposed by boundaries rectify the active driving, inducing currents. As an example, the current exterior to a fixed, elliptical inclusion asymptotically decays as r^{-2} , and the density as r^{-1} .

While [51] has shown that long-range, current-carrying solutions do exist, it is not obvious how to connect these solutions with boundary conditions. In this work, we seek to further understand ABP steady states by developing an approximation scheme that connects such asymptotic (long-range) behavior of the steady state with boundary conditions. We demonstrate the utility of this scheme by considering planar, circular, and elliptic geometries. In particular, we identify the mechanism by which certain surface-particle interactions generate long-range dipolar and quadrupolar flow fields. We verify our analytical results using two numerical methods: the first, a trajectory-sampling technique based on the stochastic particle dynamics and the second, the finite element software PDE2D (www.pde2d.com).

Our framework proves that long-range currents are tied with the breaking of detailed balance at the boundaries. We argue that this connection has far-reaching implications for nonequilibrium steady states in general, not just those in active matter. Further, our work provides insight into pathways to construct finite current steady states via the design of boundary conditions. As we provide intuitive and computationally cheap methods to connect boundary conditions to material properties in bulk, they can be used to significantly constrain the space of design possibilities to obtain such steady states. One can then harness these types of long-range density variations and spontaneous flows to engineer active baths with tunable functionality, such as 'depletion-induced' long-ranged forces between passive inclusions that can be either attractive or repulsive depending on the configuration and design [51–60].

2. Model definitions

We consider ABPs in 2D. The dynamics of the center of mass $\mathbf{r}(t) = (x(t), y(t))$ and $\hat{u} = (\cos \theta, \sin \theta)$, the direction of the self-propulsion velocity, are given by

$$\dot{\mathbf{r}} = -\xi^{-1} \nabla V(\mathbf{r}) + v_0 \hat{u} + \sqrt{2D_t} \boldsymbol{\eta}^{\mathrm{T}}$$
(1)

$$\dot{\theta} = \sqrt{2D_r}\eta^{\rm R}.\tag{2}$$

Here, ξ is the friction (units of (mass)/(time)), $V(\mathbf{r})$ is an external potential, v_0 is the magnitude of the self-propulsion velocity, and D_t and D_r are the translational and rotational diffusion coefficients. The η variables are Gaussian white noise with $\langle \eta_i(t) \rangle = 0$ and $\langle \eta_i(t) \eta_j(t') \rangle = \delta_{ij} \delta(t - t')$. In this paper, we study the steady-state statistics of equations (1) and (2) in terms of the associated Fokker-Planck equation for the probability density function $f(\mathbf{r}, \theta)$:

$$\ell \,\hat{u} \cdot \nabla f = -(\xi D_r)^{-1} \nabla \cdot [\nabla V(\mathbf{r}) f] + (D_t / D_r) \nabla^2 f + \partial_\theta^2 f \tag{3}$$

where $\ell \equiv v_0/D_r$ is a length associated with the persistence of particle trajectories in space. Previous work has used this equation as a starting point for various approximate descriptions of ABP steady states. Nevertheless, solutions that are both exact and non-trivial are essentially nonexistent. In this work, we first approximate the Fokker-Planck equation itself, isolating the effects of activity by neglecting thermal noise (setting $D_t = 0$). In addition, we let $\nabla V(\mathbf{r})$ simulate an impenetrable, passive inclusion occupying a bounded region S of \mathbb{R}^2 (figure 1). Specifically, we make $\nabla V(\mathbf{r})$ large on a narrow region defining the boundary of S (denoted ∂S), and 0 otherwise. Then, in the region exterior to S, (3) becomes

$$\ell \,\hat{u} \cdot \nabla f = \partial_{\theta}^2 f. \tag{4}$$

Mathematically, an equation of this form requires so-called 'half-range' boundary conditions on ∂S , which *only* specify the distribution of particles pointing *outward* from ∂S [61]. That is, if \hat{n} is the outward unit normal vector at a point \mathbf{r}_0 on ∂S , then $f(\mathbf{r}_0, \theta)$ is specified only where $\hat{n} \cdot \hat{u} > 0$. Physically, these boundary conditions derive

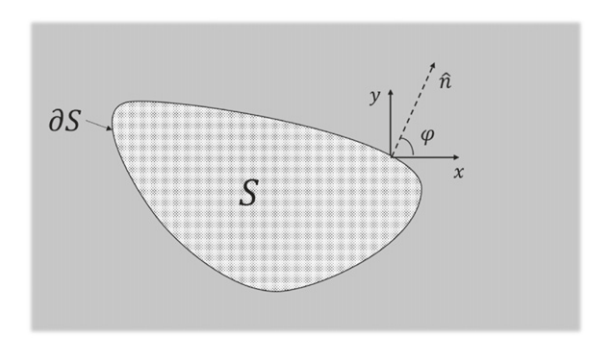


Figure 1. Illustration of the problems of interest in this work. The region S models a fixed inclusion with hard walls. The boundary ∂S is an idealized approximation of the narrow region $\mathbb B$ on which $\nabla V(\mathbf r)$ is steep and repulsive. Outside of $S, \nabla V(\mathbf r)$ is zero and the ABPs move freely with a uniform density boundary condition at infinity.

from the details of the particle-boundary interactions, which occur just within ∂S . For instance, if $\nabla V(\mathbf{r})$ is steep and repulsive, then, to a good approximation, particles leave the boundary as soon as their self-propulsion velocity points away from it, which causes $f(\mathbf{r}_0, \theta)$ to have strong peaks near $\hat{n} \cdot \hat{u} \approx 0$ and be 0 otherwise [34].

3. Review of 1D problems

Our framework for 2D problems is motivated in part by our previous treatment of 1D problems [34, 62], for which equation (4) simplifies to

$$\ell \cos \theta \frac{\partial f(x,\theta)}{\partial x} = \frac{\partial^2 f(x,\theta)}{\partial \theta^2}.$$
 (5)

Here, we consider this equation on a finite domain 0 < x < W and with boundary conditions

$$f(0,\theta) = v_{+}(\theta), \quad \text{where } \cos(\theta) > 0$$
 (6)

$$f(W, \theta) = v_{-}(\theta), \text{ where } \cos(\theta) < 0$$
 (7)

for given $v_{+}(\theta)$. Note that equations (6) and (7) conform with the type of boundary condition from section 2, with $v_{\pm}(\theta)$ being derived from the interactions of the ABPs with walls at x = 0, W.

Here, we solve this problem by separation of variables. The separable solutions take the form $e^{-r_k(x/\ell)}\phi_k(\theta)$, where

$$\frac{\mathrm{d}^2 \phi_k}{\mathrm{d}\theta^2} + (r_k \cos \theta)\phi_k = 0. \tag{8}$$

Together with periodic boundary conditions in θ , this equation is an eigenvalue problem of the indefinite Sturm-Liouville type. It can be shown that there are an infinite number

of eigenvalues that are discrete, real, and anti-symmetric about 0; we index these as

$$\dots r_{-2} < r_{-1} < r_0 < r_1 < r_2 < \dots \tag{9}$$

where $r_0 = 0$. References [34, 62] contain further details on r_k and ϕ_k and their computation.

The usual strategy is to expand the general solution in terms of the separable solutions. However, for the problem (5)-(7), the separable solutions do not span the solution space. Instead, a non-separable solution $x - \ell \cos \theta$ is required, so that the general solution is

$$f(x,\theta) = c_0 + d_0(x - \ell \cos \theta) + \sum_{k>0} a_k e^{-r_k(x/\ell)} \phi_k + \sum_{k<0} a_k e^{-r_k(x-W)/\ell} \phi_k.$$
 (10)

The problem (5)–(7) will then be solved if we can find c_0 , d_0 , and a_k , such that the boundary conditions (6) and (7) are satisfied. Specifically, this amounts to the requirement that, in addition to $c_0 + d_0(x - \ell \cos \theta)$, the positive half of the spectrum generates a complete set over the interval where $\cos \theta > 0$, and similarly for the negative half of the spectrum on $\cos \theta < 0$. For the eigenvalue problem (8), this result indeed holds [62], which solves the problem at a formal level. Practical aspects of computing the expansion coefficients are addressed in [34, 62]. For present purposes, we note that the separable solutions in (10) decay exponentially with distance from the boundary, so the behavior of equation (1) in the bulk is dominated by the remainder $c_0 + d_0(x - \ell \cos \theta)$. Therefore, if the constants c_0 and d_0 can be measured or inferred, then one obtains a significantly simplified picture of the steady-state statistics far from boundaries. Our goal in the next section is to replicate this simplification for 2D problems.

4. Method of solution for 2D problems

Motivated by equation (10), we look for a way to decompose fully 2D problems into boundary layer and bulk (asymptotic) parts. The generic existence of a boundary layer is implied by the first-order spatial gradients in (4), which suggest solutions that decay exponentially over the length scale ℓ , similarly to the separable solutions $e^{-r_k(x/\ell)}\phi_k(\theta)$ in the 1D problem. These solutions would be non-analytic in ℓ , which raises the question of whether solutions exist that are analytic in ℓ , i.e. expressible as the power series

$$f \sim f_0 + \ell f_1 + \ell^2 f_2 + \cdots$$
 (11)

Such solutions are candidates for the bulk, or asymptotic, part of the solution. Indeed, they are known to exist for a broad class of integro-differential equations, called 'transport equations', which are similar to (4) in abstract structure and model various transport phenomena [61, 63–65]. Because the asymptotic solutions (11) persist into the bulk, they function as a useful starting point for coarse-grained models. For instance, in the Boltzmann equation for dilute gases, they generate classical hydrodynamics and its extensions, e.g. the Euler, Navier–Stokes, and Burnett equations [64, 66, 67].

It is now apparent that the non-separable solution $x - \ell \cos \theta$ we introduced for 1D problems has the form of equation (11), and can be derived by substituting (11) into equation (1). In fact, we can use the same method to construct the asymptotic solution for fully 2D problems. As explained below, this solution behaves like a diffusion process, so we denote it by f_d . Substituting (11) into (4) and matching powers of ℓ gives

$$f_d(x, y, \theta) = c_0 + \ell \beta(x, y) - \ell^2 \left(\frac{\partial \beta(x, y)}{\partial x} \cos \theta + \frac{\partial \beta(x, y)}{\partial y} \sin \theta \right) + \mathcal{O}(\ell^3)$$
(12)

where c_0 is a constant and $\beta(x,y)$ is an as-yet unknown function satisfying $\nabla^2 \beta = 0$. At quadrupole order, a coordinate-free representation is

$$f_d(\mathbf{r},\theta) = c_0 + \ell \beta - \ell^2 \nabla \beta \cdot \hat{\mathbf{u}} + \frac{\ell^3}{4} (\partial_i \partial_j \beta) \hat{u}_i \hat{u}_j + \cdots$$
 (13)

By integrating equation (12) over θ , we see that $\beta(x,y)$ is proportional to the density $\rho_d(x,y)$ (minus an additive constant) and so $\nabla^2 \rho_d = 0$. Moreover, integrating against \hat{u} results in a Fickian expression for the particle flux $\mathbf{J}_d(x,y)$:

$$\mathbf{J}_d(x,y) = \int \hat{u} f_d(x,y,\theta) d\theta = -\frac{\ell^2}{2} \nabla \rho_d(x,y). \tag{14}$$

Therefore, the solution (12) has the characteristics of a diffusive process. For this reason, we call it the *diffusion solution*.

As the asymptotic part of the solution, f_d in principle provides an accurate description of ABP steady states far from boundaries. However, there is the significant caveat that the boundary conditions for $\beta(x,y)$ —and by extension f_d itself—are not known a priori. In general, it is not possible to obtain these without solving for the full distribution function, which includes the boundary layer. Addressing this challenge is one of the primary goals of this paper. Our starting point is the interesting observation that the separable solutions in the 1D problem are orthogonal to $\cos \theta$:

$$\int e^{-r_k(x/\ell)} \phi_k(\theta) \cos \theta \, d\theta = 0. \tag{15}$$

Combined with the expression for the general solution, equation (10), one obtains a simple, linear relation between the wall-normal flux $J_n = \int f(x,\theta)\cos\theta \,d\theta$ —which is independent of x—and the parameters c_0 and d_0 of the bulk solution. In particular, if J_n is known, then one can infer the bulk solution up to a normalization factor, without having to treat the boundary layer part of the solution directly. The caveat is that J_n cannot be calculated in a simple way from the boundary data on the full PDE, because these are specified only on half of the θ domain. The values on the other half can only be obtained by solving the full problem, which includes the separable solutions in (10). On the other hand, J_n itself is a physical quantity that can be estimated or measured, in which case the bulk solution is a simplified and self-contained model of the steady state far from boundaries. Our strategy is to generalize this approach to fully 2D problems. There, the flux varies with \mathbf{r} , and so we assume, at a minimum, that the

boundary-normal flux J_n is known at each point on the boundary. Here, **J** is defined as $\int \hat{u} f(\mathbf{r}, \theta) d\theta$, so that

$$J_{\rm n} \equiv \mathbf{J} \cdot \hat{n} = \int (\hat{u} \cdot \hat{n}) f(\mathbf{r}, \theta) d\theta \tag{16}$$

where \hat{n} is the outward pointing normal vector on the boundary. Ideally, the boundary layer part of the solution would be orthogonal to $\hat{u} \cdot \hat{n}$, in which case the asymptotic part f_d would carry all the wall-normal flux. Then, the unknown function $\beta(x,y)$ in the expression for f_d (equation (12)) would satisfy $\hat{n} \cdot \mathbf{J} = \hat{n} \cdot \nabla \beta$ on the boundary, i.e. acquire a Neumann boundary condition. Because $\beta(x,y)$ is also constrained to satisfy Laplace's equation $\nabla^2 \beta = 0$, knowing $\hat{n} \cdot \mathbf{J}$ would uniquely determine $\beta(x,y)$ (up to an additive constant) and thereby the entirety of the asymptotic solution, equation (12). In reality, the situation is not so simple: as we show in section 5, the boundary layer contribution to the solution is no longer guaranteed to be orthogonal to $\hat{u} \cdot \hat{n}$. In the same section, nevertheless, we provide evidence that orthogonality does hold approximately in situations where the boundary data do not vary too rapidly with ℓ . We therefore build our approach using the following approximation.

Diffusion approximation. The diffusion solution $f_d(\mathbf{r}, \theta)$ carries all the particle flux normal to the boundary, that is,

$$\int \left[f(\mathbf{r}, \theta) |_{\mathbf{r} \in \partial S'} - f_d(\mathbf{r}, \theta) |_{\mathbf{r} \in \partial S'} \right] (\hat{u} \cdot \hat{n}) d\theta = 0; \quad \to \quad \hat{n} \cdot \mathbf{J} = \hat{n} \cdot \mathbf{J}_d$$
 (17)

where \hat{n} is the unit normal vector at a point on the boundary, and $f(\mathbf{r}, \theta)$ is the full solution to the problem. \mathbf{J} and \mathbf{J}_d correspond respectively to the fluxes associated with the full solution and the diffusion solution.

Note that this approximation says nothing about the flux component parallel to the boundary. In fact, the diffusion solution for the 1D problem does not make any contribution to this component, so for 2D problems there is no rationale for an approximation like equation (17) given in terms of the parallel flux. On the other hand, the diffusion solution does give the complete flux vector far from the boundaries, from equations (12) or (14). It is in this sense that equation (17) connects long-range fluxes with the breaking of detailed balance at the boundaries, that is, a boundary normal flux that is not strictly 0. Formally,

- (a) A system breaks detailed balance at the boundary if J_n is not strictly 0.
- (b) By equation (17), this leads to a nonzero Neumann boundary condition on $\beta(x,y)$.
- (c) Because $\beta(x, y)$ itself satisfies Laplace's equation, it will be non-constant in such a case (and long-ranged via its multipole expansion).
- (d) By equations (12) and (14), the density and current will also be long-ranged in this sense.

In the following sections, we work out this method of solution in detail for a selection of problems, corresponding to planar, circular, and elliptic geometries. Along with validating the diffusion approximation, we show that it is possible to obtain reasonable a priori estimates of the boundary normal flux $\hat{n} \cdot \mathbf{J}$ in physically relevant situations.

5. Benchmarking the framework: planar geometry

As a first step, we validate our assertion that the diffusion approximation captures the bulk properties of the ABPs in the presence of boundaries. We do this by comparing the diffusion approximation with an exact solution to the planar 2D problem. Specifically, we consider a system with a wall at x = 0 and solve for the steady-state distribution $f(x, y, \theta)$ in the region $0 < x < \infty$ and $-\infty < y < \infty$ with boundary conditions

$$f(0, y, \theta) = q(y, \theta), \text{ where } \cos \theta > 0$$
 (18)

$$f(x, y, \theta) \to 0$$
, as $x \to \infty$. (19)

To simplify notation, we work in units where $\ell = 1$.

5.1. Separation of variables

In the Cartesian coordinates relevant for this problem, equation (4) is separable. Taking $f = \Gamma(x) \Xi(y)\Theta(\theta)$ leads to

$$\frac{\mathrm{d}\Gamma}{\mathrm{d}x} + \lambda\Gamma = 0; \qquad \frac{\mathrm{d}\Xi}{\mathrm{d}y} + \nu\Xi = 0 \tag{20}$$

$$\frac{\mathrm{d}^2\Theta}{\mathrm{d}\theta^2} + (\lambda \cos \theta + \nu \sin \theta)\Theta = 0 \tag{21}$$

where λ and ν are constants. To satisfy the general y-dependence of the boundary condition x=0, the functions $\Xi(y)$ need to be complete on $-\infty < y < \infty$. Thus, we take ν to be purely imaginary but otherwise unconstrained, writing $\nu = \mu i$, where μ is real. We hope that for each μ , equations (20) and (21) admit a sequence of eigenvalues $\lambda_k(\mu)$ and eigenfunctions $\Theta_k(\theta,\mu)$, which are complete in θ .

5.2. Diffusion solutions

Let us now consider the asymptotic solution in the diffusion approximation formulated above,

$$f_d(x, y, \theta) = c_0 + \epsilon \beta(x, y) - \epsilon^2 \left(\cos \theta \frac{\partial \beta(x, y)}{\partial x} + \sin \theta \frac{\partial \beta(x, y)}{\partial y} \right) + \mathcal{O}(\epsilon^3)$$
 (22)

where $\nabla^2 \beta(x,y) = 0$. We anticipate separable solutions with a (x,y) dependence of the form $e^{c x} e^{\pm icy}$, where c is a constant. This suggests taking $\lambda = \pm \mu$ in equations (20) and (21). Equation (21) then becomes

$$\frac{\mathrm{d}^2\Theta}{\mathrm{d}\theta^2} \pm \mu \,\mathrm{e}^{\pm\mathrm{i}\theta}\Theta = 0. \tag{23}$$

Making the change of variable $u = 2i(\pm \mu)^{1/2} e^{\pm i\theta/2}$, this turns into

$$u^2 \frac{\mathrm{d}^2 \Theta}{\mathrm{d}u^2} + u \frac{\mathrm{d}\Theta}{\mathrm{d}u} + u^2 \Theta = 0 \tag{24}$$

which is Bessel's equation with order 0. The periodic boundary condition in θ implies $\Theta(u) = \Theta(-u)$, and thus the desired solution is the Bessel function of the first kind $J_0(u)$. In summary, the functions

$$f_d(x, y, \theta, \mu) = e^{\mp \mu x} e^{-\mu i y} J_0 \left(2i(\pm \mu)^{1/2} e^{\pm i \theta/2} \right)$$
 (25)

are solutions of (4) for any real μ . A direct calculation from (13) shows that these are indeed the diffusion solutions.

5.3. Boundary layer solutions

Now, in order to construct the exact solution, we need to tackle the boundary layer, and this is difficult to calculate. Let us begin by making the following change of variables, $(\lambda, \mu) = (r \cos \gamma, -ir \sin \gamma)$, where λ, μ , and r are real and γ is complex. Substitution into (21) gives

$$\frac{\mathrm{d}^2\Theta}{\mathrm{d}\omega^2} + (r\cos\omega)\Theta = 0 \tag{26}$$

where $\omega = \theta - \gamma$ and this equation needs to be solved with periodic boundary conditions. Equation (26) has the same form as equation (8) describing the angular eigenfunctions for 1D problems. We recall that there are an infinite number of eigenvalues that are discrete, real, and anti-symmetric about 0, which we indexed with k according to $\ldots r_{-2} < r_{-1} < r_0 < r_1 < r_2 < \ldots$, where $r_0 = 0$. Thus, the spectrum of the two-parameter problem (21) can be expressed as

$$\lambda_k(\mu) = \operatorname{sgn}(k)\sqrt{|r_k|^2 + \mu^2}, \quad k \in \mathbb{Z} \setminus \{0\}$$
(27)

$$\lambda_0^{\pm}(\mu) = \pm |\mu|. \tag{28}$$

We denote the corresponding eigenfunctions as $\Theta_k(\theta, \mu)$ and $\Theta_0^{\pm}(\theta, \mu)$. Like the $\mu = 0$ case, the spectrum is discrete, real, and anti-symmetric about 0. Nevertheless, there are important differences. While the eigenvalues $\lambda_k(\mu)$ are real, the eigenfunctions $\Theta_k(\theta, \mu)$ are not. In addition, 0 is no longer an eigenvalue for nonzero μ . Instead, the null space of the $\mu = 0$ problem transforms into the space spanned by $\Theta_0^{\pm}(\theta,\mu)$, which are the diffusion solutions from the previous section. Explicitly,

$$\Theta_0^{\pm}(\theta,\mu) = J_0 \left(2i|\mu|^{1/2} e^{\pm \operatorname{sgn}(\mu)i\theta/2} \right)$$
(29)

such that the diffusion solutions are

$$f_d(x, y, \theta, \mu) = e^{\mp |\mu| x} e^{-\mu i y} \Theta_0^{\pm}(\theta, \mu).$$
 (30)

Using the change of variable from the previous section, the $\Theta_k(\theta, \mu)$ for $k \neq 0$, $\mu \neq 0$ can be constructed through analytic continuation of the known eigenfunctions for $\mu = 0$.

Reference [34] represents the latter as an even/odd Fourier series:

$$\Theta_{k}(\omega, 0) = \begin{cases} \frac{A_{0}^{(k)}(0)}{2} + \sum_{m=1}^{\infty} A_{m}^{(k)}(0) \cos m\omega & k \text{ even} \\ \sum_{m=1}^{\infty} A_{m}^{(k)}(0) \sin m\omega & k \text{ odd.} \end{cases}$$
(31)

The coefficients $A_n^{(k)}(0)$ are real and can be computed as eigenvectors of an infinite tridiagonal matrix [34]. We adopt the following normalization convention:

$$\int_{-\pi}^{\pi} \Theta_k(\omega, 0)^2 \cos \omega \, d\omega = \operatorname{sgn}(k); \quad \Theta_k(\omega + \pi, 0) = \Theta_{-k}(\omega, 0)$$
(32)

which also fixes the normalization on $\Theta_k(\omega, \mu)$ for general μ . Next, changing variable $\omega \to \theta - \gamma$ gives

$$\Theta_{k}(\theta - \gamma, 0) = \begin{cases} \frac{A_{0}^{(k)}(\mu)}{2} + \sum_{m=2}^{\infty} A_{m}^{(k)}(\mu) \cos m\theta + \sum_{m=2}^{\infty} B_{m}^{(k)}(\mu) \sin m\theta & k \text{ even} \\ -\sum_{m=1}^{\infty} B_{m}^{(k)}(\mu) \cos m\theta + \sum_{m=1}^{\infty} A_{m}^{(k)}(\mu) \sin m\theta & k \text{ odd} \end{cases}$$
(33)

where

$$A_n^{(k)}(\mu) = \cos\left[n \arctan\left(\operatorname{sgn}(k)\frac{\mathrm{i}\mu}{\sqrt{|r_k|^2 + \mu^2}}\right)\right] \cdot A_n^{(k)}(0) \tag{34}$$

$$B_n^{(k)}(\mu) = \sin\left[n \arctan\left(\operatorname{sgn}(k)\frac{\mathrm{i}\mu}{\sqrt{|r_k|^2 + \mu^2}}\right)\right] \cdot A_n^{(k)}(0). \tag{35}$$

One can check by substitution that (33) gives solutions of equation (21). So, we make the association

$$\Theta_k(\theta - \gamma, 0) = \Theta_k(\theta, \mu). \tag{36}$$

5.4. Full solution of a boundary value problem

To construct a general solution to the 2D planar problem, the separable solutions must satisfy some completeness relations in the θ variable. Towards this end, it is reasonable to expect that the $\Theta_k(\theta, \mu)$ for $\mu \neq 0$ satisfy full- and half-range completeness theorems analogous to those which hold for the $\mu = 0$ eigenfunctions. Numerical evidence suggests that such theorems hold for the real part of the Θ_k , denoted by Ω_k [65]:

$$\Omega_k(\theta, |\mu|) \equiv \Re\left[\Theta_k(\theta, \mu)\right] = \frac{\Theta_k(\theta, \mu) + \Theta_k(\theta, -\mu)}{2}$$
(37)

where we have used the fact that $\Theta_k(\theta, -\mu)$ is the complex conjugate of $\Theta_k(\theta, \mu)$. To formulate the completeness conjectures, let \mathscr{H} be the Hilbert space associated with the inner product $\langle f, g \rangle = \int_{-\pi}^{\pi} f(\theta) g(\theta) |\cos \theta| \, \mathrm{d}\theta$, and let \mathscr{H}_{\pm} be the respective subspaces where $\cos \theta > 0$ or $\cos \theta < 0$. Then, we conjecture the following:

- Full-range completeness. For real and non-zero μ , any real-valued function in \mathscr{H} can be expanded in terms of the functions $\{\Omega_k(\theta, |\mu|), \Omega_0^{\pm}(\theta, |\mu|)\}$, where $k \in \mathbb{Z} \setminus \{0\}$.
- Half-range completeness. For real and non-zero μ , any real-valued function in \mathcal{H}_+ can be expanded in terms of the functions $\{\Omega_k(\theta,|\mu|),\Omega_0^+(\theta,|\mu|)\}$, where k>0. Similarly, any real-valued function in \mathcal{H}_- can be expanded in terms of $\{\Omega_k(\theta,|\mu|),\Omega_0^-(\theta,|\mu|)\}$, where k<0

Interestingly, the imaginary part of Θ_k does not appear to share the completeness properties of the real part. As explained below and in appendix B, however, both real and imaginary parts are required for solving the full boundary value problem. In anticipation of this, we introduce a similar shorthand notation as for the real part:

$$\Upsilon_k(\theta, |\mu|) \equiv \Im\left[\Theta_k(\theta, \mu)\right] = \frac{\Theta_k(\theta, \mu) - \Theta_k(\theta, -\mu)}{2i}.$$
 (38)

Now, our task is to express $f(x, y, \theta)$ as a linear combination of separable solutions from above, varying λ and μ over the range of allowed values. In view of the asymptotic condition on f, λ must be positive, which restricts us to half of the spectrum. We then have

$$f(x, y, \theta) = \int_{-\infty}^{\infty} d\mu \left[\sum_{k \geqslant 0} a_k(\mu) e^{-\lambda_k(\mu)x} \Theta_k(\theta, \mu) \right] e^{-i\mu y}$$
(39)

where the k=0 mode corresponds to the sign of μ , i.e. $\Theta_0 = \Theta_0^{\text{sgn}(\mu)}$ and $\lambda_0(\mu) = \text{sgn}(\mu)\mu$. Since the boundary condition $g(y,\theta)$ is real-valued, it is convenient to separate everything into real and imaginary parts. For compactness, we do not write the explicit μ and θ arguments on the Ω_k and Υ_k (each has arguments $+\theta$ and $|\mu|$). Then,

$$f(x,y,\theta) = \int_{0}^{\infty} d\mu \sum_{k\geqslant 0} \left\{ +\Re\left[a_{k}(\mu)\right] \Omega_{k} - \Im\left[a_{k}(\mu)\right] \Upsilon_{k} + \Re\left[a_{k}(-\mu)\right] \Omega_{k} + \Im\left[a_{k}(-\mu)\right] \Upsilon_{k} \right\} e^{-\lambda_{k}x} \cos \mu y$$

$$+ \int_{0}^{\infty} d\mu \sum_{k\geqslant 0} \left\{ +\Re\left[a_{k}(\mu)\right] \Upsilon_{k} + \Im\left[a_{k}(\mu)\right] \Omega_{k} + \Re\left[a_{k}(-\mu)\right] \Upsilon_{k} - \Im\left[a_{k}(-\mu)\right] \Omega_{k} \right\} e^{-\lambda_{k}x} \sin \mu y$$

$$+ i \int_{0}^{\infty} d\mu \sum_{k\geqslant 0} \left\{ +\Re\left[a_{k}(\mu)\right] \Upsilon_{k} + \Im\left[a_{k}(\mu)\right] \Omega_{k} - \Re\left[a_{k}(-\mu)\right] \Upsilon_{k} + \Im\left[a_{k}(-\mu)\right] \Omega_{k} \right\} e^{-\lambda_{k}x} \cos \mu y$$

$$+ i \int_{0}^{\infty} d\mu \sum_{k\geqslant 0} \left\{ -\Re\left[a_{k}(\mu)\right] \Omega_{k} + \Im\left[a_{k}(\mu)\right] \Upsilon_{k} + \Re\left[a_{k}(-\mu)\right] \Omega_{k} + \Im\left[a_{k}(-\mu)\right] \Upsilon_{k} \right\} e^{-\lambda_{k}x} \sin \mu y$$

$$+ i \int_{0}^{\infty} d\mu \sum_{k\geqslant 0} \left\{ -\Re\left[a_{k}(\mu)\right] \Omega_{k} + \Im\left[a_{k}(\mu)\right] \Upsilon_{k} + \Re\left[a_{k}(-\mu)\right] \Omega_{k} + \Im\left[a_{k}(-\mu)\right] \Upsilon_{k} \right\} e^{-\lambda_{k}x} \sin \mu y$$

$$(40)$$

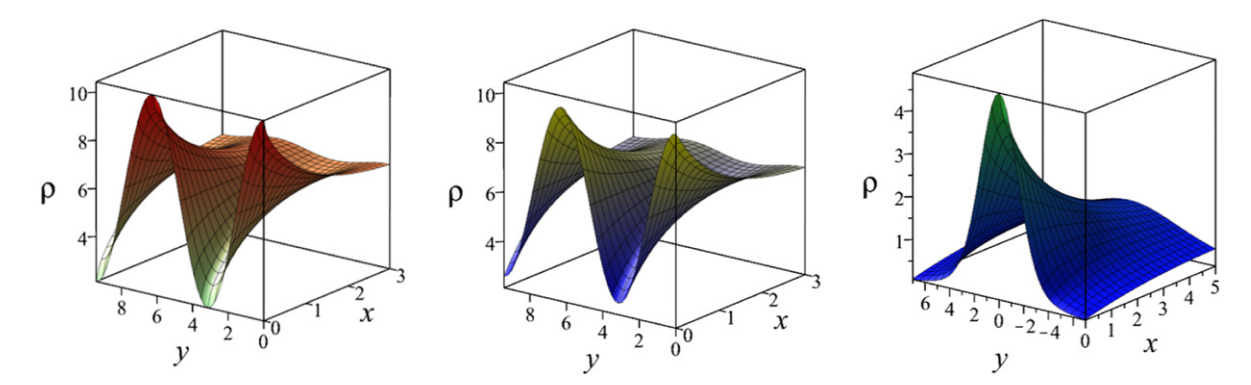


Figure 2. Densities for the planar problem with two example boundary conditions. (Left and middle) $f(0, y, \theta) = 2 + \cos y$, with the left displaying the density $\rho(x, y)$ computed using (40) and the least-squares method and the middle showing the density contribution from the diffusion solution, $\rho_d(x, y) \simeq 3.693 \times e^{-x} \cos y$. The two qualitatively agree, validating the diffusion approximation. (Right) $f(0, y, \theta) = e^{-y^2/4}$, density computed using the least squares method. Compared to the left panel, this illustrates the strong influence of the boundary on the bulk solution.

where the k = 0 mode is the positive one, i.e. $\Omega_0 = \Omega_0^+$ and $\Upsilon_0 = \Upsilon_0^+$. By comparison, the first boundary condition can similarly be expressed as a Fourier integral:

$$f(0, y, \theta) = g(y, \theta) = \int_0^\infty d\mu \, q(\mu, \theta) \cos \mu y + \int_0^\infty d\mu \, p(\mu, \theta) \sin \mu y, \quad \cos \theta > 0.$$
 (41)

The problem is solved if, for given $\mu > 0$, we can choose $a_k(\mu)$ such that the quantities in brackets in equation (40) match the respective functions $q(\theta, \mu)$ and $p(\theta, \mu)$. This results in four independent equations with four independent sets of coefficients: $\Re [a_k(\pm \mu)]$ and $\Im [a_k(\pm \mu)]$. We solve these equations using a least-squares technique that appears to depend on the completeness of the Ω_k but also requires use of the Υ_k . The validity of the procedure is supported by good numerical convergence on a variety of test functions (see appendix B and [65]).

Here, we show results for the cases $g(y, \theta) = 2 + \cos y$ and $g(y, \theta) = e^{-y^2/4}$. The first boundary condition could model ABPs in an infinite channel whose walls have periodically varying absorption energies, whereas the second describes perfectly absorbing walls in the presence of a steady particle source centered around y = 0. The densities corresponding to these scenarios are shown in figure 2. As the first boundary condition involves only a single mode of the set of y eigenfunctions, the diffusion solution is easy to write down:

$$f_d(x, y, \theta) \simeq 1.176 \cdot e^{-x} \left(\Re[J_0(2i e^{i\theta/2})] \cos y + \Im[J_0(2i e^{i\theta/2})] \sin y \right).$$
 (42)

The density is just $\rho_d(x, y) \simeq 3.693 \cdot e^{-x} \cos y$, which compares well with the exact solution (see figure 4).

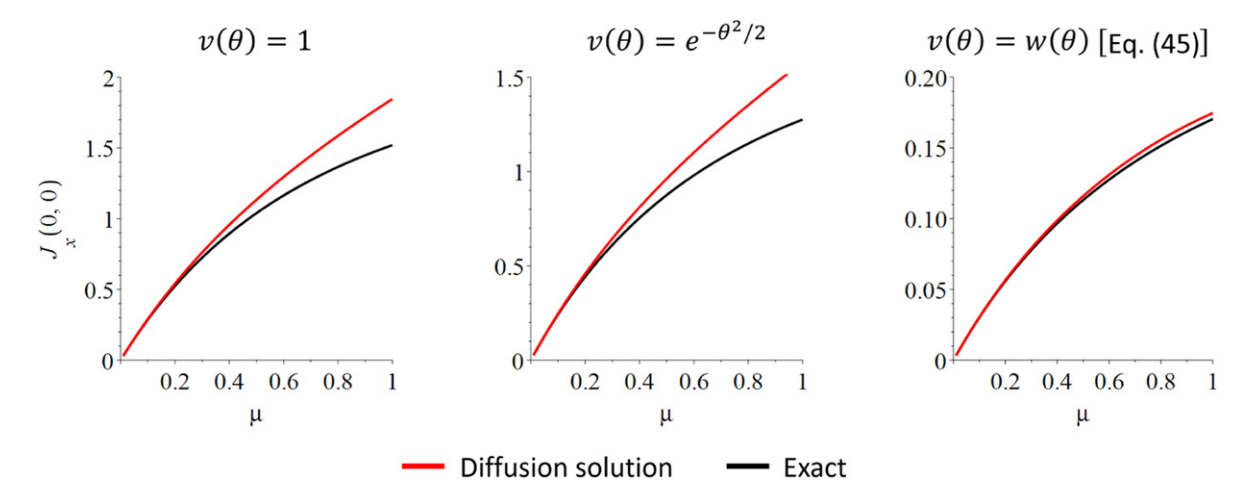


Figure 3. The diffusion approximation says that the diffusion solution carries all of the normal flux at the boundary. Our first and most basic test of this approximation is for the single μ -eigenmode boundary condition $f(0, y, \theta) = v(\theta)\cos\mu y$ in the planar geometry. We find satisfactory agreement for $\mu \ll 1$ ($\mu \ll \ell^{-1}$ in dimensionful form). This supports our claim that the diffusion approximation is valid so long as the length characterizing the variation of the boundary data (μ^{-1} in this case) is large compared with ℓ . Since the solution for a general boundary condition $f(0, y, \theta) = g(y, \theta)$ is a sum over single- μ eigenmodes (equation (39)), we expect this conclusion to translate to more general problems as well; see figure 4 for examples.

5.5. Validation of the diffusion approximation

The validity of the diffusion approximation depends on whether the diffusion solution carries most of the boundary normal flux. The explicit construction of the boundary layer in section 5.3 allows us to test this assumption directly. Working from the representation (33), we find

$$\int_{-\pi}^{\pi} \Theta_{k}(\theta, \mu) \begin{bmatrix} \sin \theta \\ \cos \theta \end{bmatrix} d\theta = \begin{cases}
\begin{bmatrix} 0 \\ 0 \end{bmatrix} & k \text{ even (and nonzero)} \\
\frac{\pi A_{1}^{(k)}(0)}{r_{k}} \begin{bmatrix} \sqrt{|r_{k}|^{2} + \mu^{2}} \\ -i\mu \end{bmatrix} & k \text{ odd.}
\end{cases}$$
(43)

Crucially, equation (43) tells us that the boundary normal flux contained in the boundary layer solutions is at most $\mathcal{O}(\mu)$, i.e.

$$\int (\text{boundary layer})(\hat{n} \cdot \hat{u}) d\theta = \int (\text{boundary layer}) \cos \theta d\theta = \mathcal{O}(\mu). \tag{44}$$

Because μ is the wavenumber of the y-dependent part of the boundary layer (in units of ℓ), it follows that the assumptions of the diffusion approximation are violated, at most, to order $\mathcal{O}(\ell/L_b)$, where L_b is the length scale describing the variation of the boundary data with y. We have tested this conclusion numerically for a selection of boundary conditions. Notably, with the analytic solution (40) in hand, it is possible to

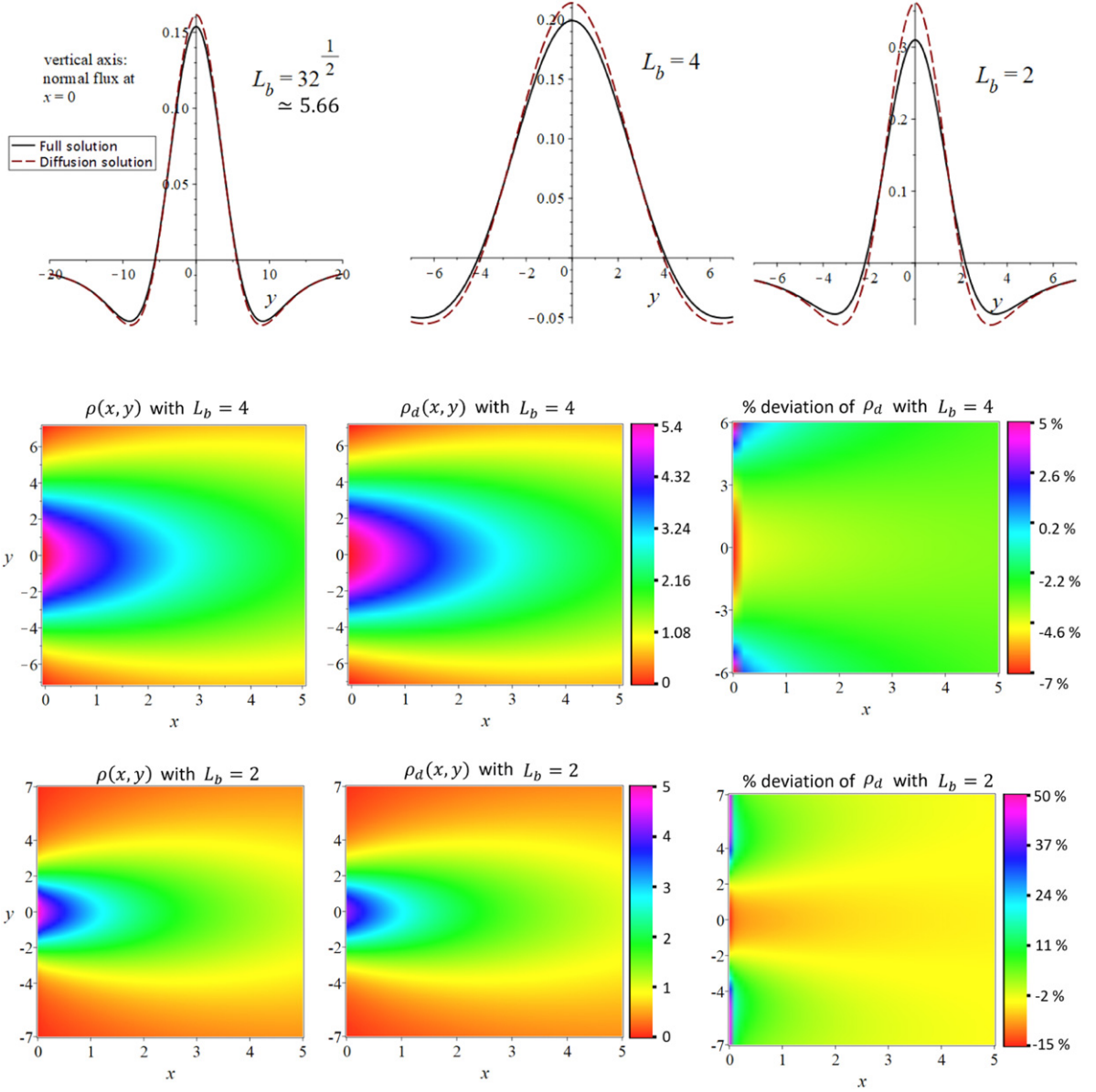


Figure 4. Tests of the diffusion approximation in the planar geometry with boundary condition $f(0, y, \theta) = e^{-y^2/L_b^2}$. The top row shows the normal flux at x = 0. The diffusion solution indeed carries most of the flux for $L_b > 1$, with the fraction increasing with L_b . This supports our claim that the diffusion approximation is valid so long as the length characterizing the variation of the boundary data (L_b in this case) is large compared with ℓ . In the bottom two rows, we compare the density calculated in the diffusion approximation (ρ_d) with the exact density (ρ). As expected, the approximation increases in accuracy as L_b becomes large compared with ℓ .

analytically separate the diffusion solution from the boundary layer and test the diffusion approximation directly, which is not possible for other geometries considered later. First, we consider the boundary condition $g(y, \theta) = v(\theta)\cos\mu y$ corresponding to a single mode

of the set of y eigenfunctions. The solution for general boundary conditions will be a sum over modes of this form, via equation (40). Thus, knowing how the accuracy of the diffusion approximation varies with μ will allow us to judge its accuracy for general problems as well. Towards this end, figure 3 compares the exact normal flux J_x with the flux of the diffusion solution alone, for three different $v(\theta)$: $v(\theta) = 1$, $e^{-\theta^2/2}$, and

$$v(\theta) = \left(\left(\frac{\pi}{2} \right)^2 - \theta^2 \right) \cdot \left(e^{-5(\theta - 1.5)^2} + e^{-5(\theta + 1.5)^2} \right) \equiv w(\theta)$$
 (45)

where $w(\theta)$ is chosen to be representative of a smooth function peaked near $\pm \pi/2$. In all cases, the approximation is good for $\mu \ll 1$, whereas for $\mu > 1$ the accuracy deteriorates. Thus, the diffusion approximation should work well for boundary conditions that vary slowly with respect to y, corresponding to $\mu \ll 1$. Physically, if L_b is the length scale describing the boundary variations, then we require $L_b \gg \ell$. On the other hand, modes with $\mu \gg 1$ decay rapidly away from the boundary, so we might expect the diffusion approximation to fare reasonably even when a small number of modes with $\mu > 1$ are present.

To test these conclusions, we next consider the boundary condition $g(y,\theta) = e^{-y^2/L_b^2}$. Figure 4 compares the exact normal flux J_x with the flux of the diffusion solution alone for $L_b = 2, 4, 32^{1/2}$. As predicted, the two quantities coincide with high accuracy for $L_b \gg \ell = 1$, and even when $L_b \sim 1$, the agreement is at least qualitative. Figure 4 also compares the density from the diffusion approximation with the exact density. As expected, the agreement is poor near x = 0, where the boundary layer contribution is significant. Far from the boundary, there are still systematic deviations, but of a lesser degree: around 5% relative error for $L_b = 4$ and 10% for $L_b = 2$. Moreover, since the deviations are systematic, the qualitative agreement is good. We conclude that the diffusion approximation gives a semi-quantitative picture of the asymptotic density for boundary variations on the order of ℓ .

6. Illustration 1: circular geometry

6.1. Problem statement

We define polar coordinates (r, α) by $x = r \cos \alpha$ and $y = r \sin \alpha$. Applying this transformation to equation (4) gives

$$\cos(\alpha - \theta) \frac{\partial f}{\partial r} - \frac{\sin(\alpha - \theta)}{r} \frac{\partial f}{\partial \alpha} = \frac{\partial^2 f}{\partial \theta^2}.$$
 (46)

In a geometry that is radially symmetric, f depends on α and θ only through the combination $\phi \equiv \alpha - \theta$. Then, (46) simplifies to

$$\cos \phi \frac{\partial f}{\partial r} - \frac{\sin \phi}{r} \frac{\partial f}{\partial \phi} = \frac{\partial^2 f}{\partial \phi^2} \tag{47}$$

where $-\pi < \phi < \pi$. Perhaps surprisingly, neither of these equations are separable. More generally, we have not found equation (4) to be separable in any spatial coordinates

besides rectangular. Thus, the diffusion approximation is essential for analyzing even simple curvilinear geometries, since the boundary layer can no longer be accessed via a separation of variables.

In this section, we solve the above equations with a variety of boundary conditions. First, we consider an annular region $R_1 < r < R_2$, in which case the boundary conditions take the form

$$f(R_1, \alpha, \theta) = B_1(\alpha, \theta) \quad \text{where cos } \phi > 0$$
 (48)

$$f(R_2, \alpha, \theta) = B_2(\alpha, \theta)$$
 where $\cos \phi < 0$. (49)

We consider both spherically symmetric and non-symmetric boundary data, focusing on the qualitative differences between the solutions in either case. Second, we consider the infinite exterior region $r > R_1$, in which case the second boundary condition is replaced by $\lim_{r\to\infty} f(r,\alpha,\theta) = \text{constant}$.

6.2. Diffusion solution

The diffusion solution in the spherically symmetric case of (47) is easy to calculate:

$$f_d(r,\phi) = a + b \left(\ln r - \sum_{m=1}^{\infty} \frac{1}{m! \, m} \frac{\cos m\phi}{r^m} \right) \tag{50}$$

$$\equiv a + b g(r, \phi) \tag{51}$$

where a and b are constants. Note that since (47) is effectively a 1D problem, the most general diffusion solution contains only two undetermined constants [68, 69]. In the absence of spherical symmetry, the problem is of course more complicated and, in this case, to quadrupole order, we have

$$f_d(r,\alpha,\theta) = c_0 + \beta - \frac{\partial \beta}{\partial r} \cos \phi + \frac{1}{r} \frac{\partial \beta}{\partial \alpha} \sin \phi + \frac{\partial^2 \beta}{\partial r^2} \cos 2\phi + \frac{1}{r} \frac{\partial^2 \beta}{\partial r \partial \alpha} \sin 2\phi + \cdots$$
(52)

where $\phi = \alpha - \theta$ and $\beta(r, \alpha)$ solves $\nabla^2 \beta = 0$. With this in mind, we introduce a multipole expansion for the density ρ :

$$\frac{\rho(r,\alpha)}{2\pi} = c_0 + \beta(r,\alpha) \equiv c_0 - \frac{\boldsymbol{p} \cdot \hat{r}}{r} + \frac{Q_{ij}\hat{r}_i\hat{r}_j}{r^2} + \mathcal{O}\left(\frac{1}{r^3}\right)$$
(53)

where the constant term has been absorbed into c_0 , and p and Q are determined from the boundary conditions on $\beta(r, \alpha)$.

6.3. Symmetric circular geometry

In the case of spherical symmetry, the diffusion approximation is exact. The reason can be understood by integrating equation (47) with respect to ϕ , which gives

$$\hat{r} \cdot \mathbf{J} = \int f \cos \phi \, \mathrm{d}\phi = \frac{\mathrm{constant}}{r}.$$
 (54)

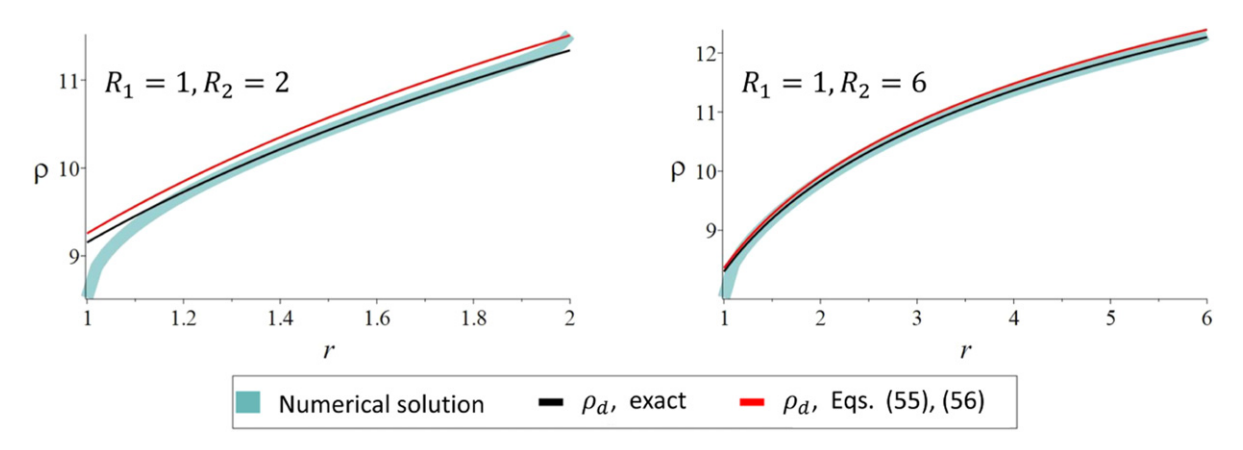


Figure 5. Density profiles for the symmetric annular problem (boundary conditions (48) and (49) with $B_1 = 1$ and $B_2 = 2$).

Comparing with (50), we see that the diffusion solution also has this property. On the other hand, the boundary layer part of the solution decays exponentially with r away from the boundary, and therefore cannot contribute to the overall flux without violating (53). Thus, the diffusion approximation is exact, and the constant b in (51) is equal to $-(\hat{r} \cdot \mathbf{J})/\pi$. Figure 5 compares the density $\rho_d(r)$ obtained in this way with a finite-element solution from PDE2D, verifying its accuracy in the bulk of the region.

An alternate (though approximate) approach estimates the solution directly in terms of the boundary functions B_1 and B_2 , and therefore does not require prior knowledge of $\hat{r} \cdot \mathbf{J}$. The idea is to choose a and b such that the boundary conditions are satisfied 'in the mean' with respect to weight functions $\cos \phi$ and $\cos^2 \phi$:

$$\int_{\cos \phi > 0} \left[B_1(\phi) - f_d(R_1, \phi) \right] \cos \phi \, d\phi + \int_{\cos \phi < 0} \left[B_2(\phi) - f_d(R_2, \phi) \right] \cos \phi \, d\phi = 0$$
 (55)

$$\int_{\cos \phi > 0} \left[B_1(\phi) - f_d(R_1, \phi) \right] \cos^2 \phi \, d\phi + \int_{\cos \phi < 0} \left[B_2(\phi) - f_d(R_2, \phi) \right] \cos^2 \phi \, d\phi = 0.$$
 (56)

As shown in figure 5, this approximation agrees well with the numerical solution. In fact, in a 1D planar geometry, this approximation is the first term in a convergent iterative scheme [62], and so we expect it to be generally valid for large R_1 and $R_2 - R_1$.

6.4. Asymmetric circular geometry

In contrast with a spherically symmetric geometry, asymmetric boundary conditions can generate currents and long-range density variations (figure 6). In a system of ABPs, one way to achieve this is with a fixed, spherical inclusion which attracts and binds particles on one side but is purely repulsive on the other side. Then, particles can escape only from one side of the sphere. For concreteness, suppose that the side with binding interactions

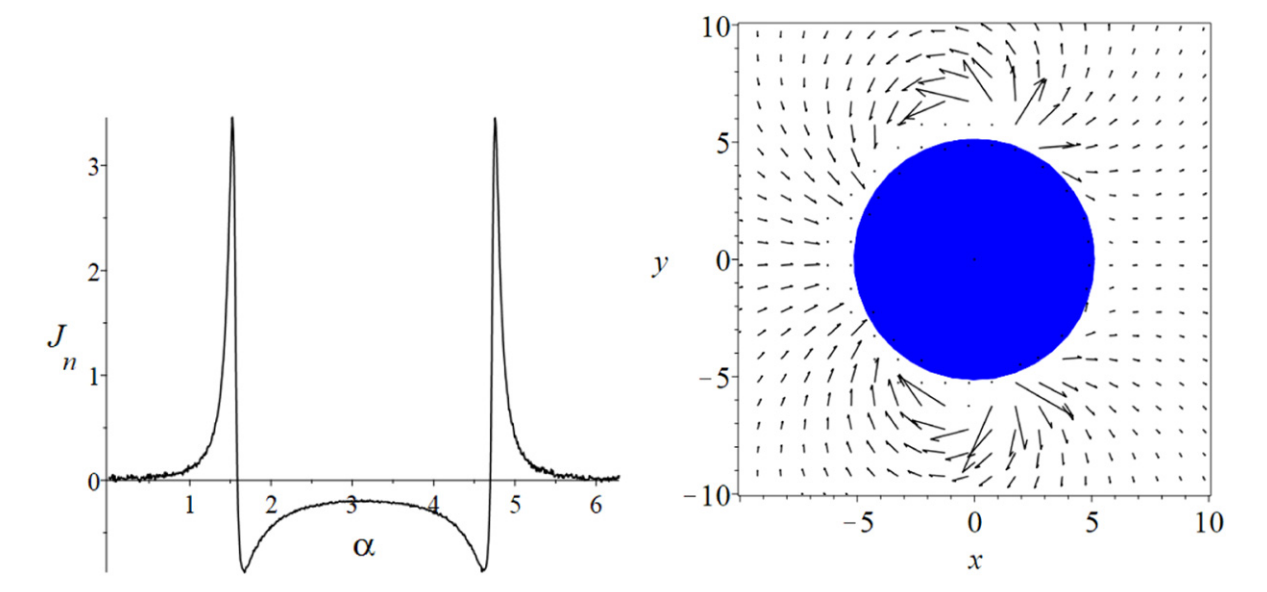


Figure 6. In a closed system of ABPs in steady state, particle-surface interactions that break spherical symmetry are sufficient to induce current loops that begin and end on different points of the boundary. This figure shows the results for one such system, in which the particle-surface interactions with a spherical inclusion are derived from a continuous, time-independent potential energy function (see equation (57), and a detailed explanation in appendix A). Qualitatively, this interaction potential has the effect of binding particles on the left side of the boundary and releasing them on the right side. The left plot shows the normal flux J_n at the boundary (black points) as a function of the angle α with respect to the x-axis. The right panel shows the flux field as a vector plot, with length of the arrows proportional to the value of the flux at the point. (Flux vectors above a certain threshold magnitude were excluded to improve visualization.)

is the left side, where x < 0. Then the boundary conditions are

$$f(R, \alpha, \theta) = \begin{cases} g_{+}(\alpha, \theta) & \text{where } \cos \alpha > 0 & \text{and} & \cos(\theta - \alpha) > 0 \\ 0 & \text{where } \cos \alpha < 0 & \text{and} & \cos(\theta - \alpha) > 0 \end{cases}$$
 (57)
unspecified else

$$\lim_{r \to \infty} f(r, \alpha, \theta) = c_0 = \text{constant}$$
(58)

such that $g_{+}(\alpha, \theta)$ gives the 'exit distribution' of particles leaving the right side of the sphere. (Since the particles are bound to the left side of the sphere, the corresponding exit distribution there is 0.) Note that $g_{+}(\alpha, \theta)$ covers only half of the (α, θ) domain. In fact, on the left side of the sphere, $f(R, \alpha, \theta)$ is nonzero on the complement of the interval where it is 0 (the 'entrance distribution'). However, only the exit distribution in equation (57) is required to form a well-posed boundary-value problem (see section 2).

While the exit distribution is exactly 0 on the left side of the sphere, the corresponding distribution $g_{+}(\alpha, \theta)$ on the right side depends on the statistics of particle

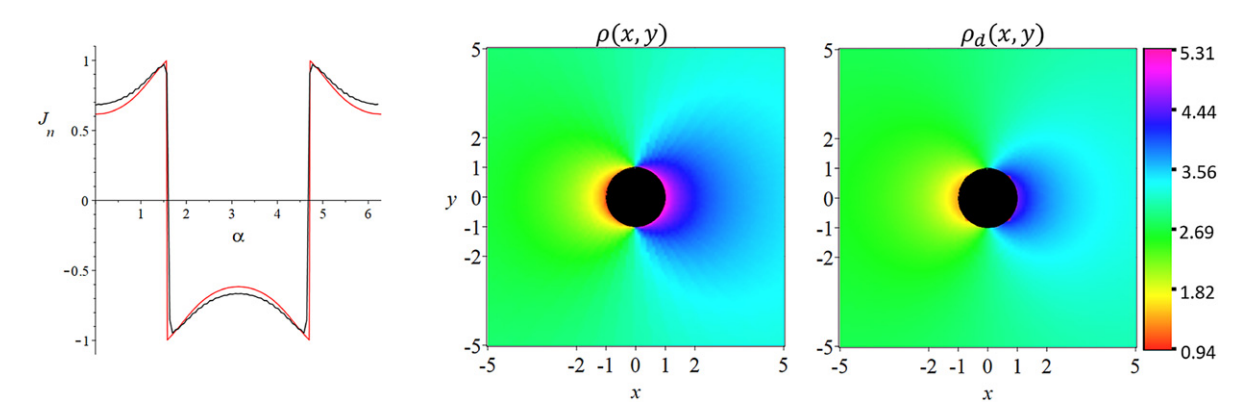


Figure 7. Tests of our analytical predictions for boundary conditions (57) and (58) with R=1 and $g_+=1$. The left plot compares the boundary normal flux $J_{\rm n}$ from the finite element solution (black points) with the analytical result (red curve) from the locally planar analysis in appendix C. The other two plots compare the particle density in the diffusion approximation (ρ_d , middle plot) with the finite-element solution (ρ , left plot). The agreement is quite good given that the analytical approximations have no free parameters.

trajectories in the vicinity of the sphere, and requires a more detailed analysis that we do not attempt here. For example, one would need to calculate the probability that a trajectory starting on the left side of the sphere would eventually depart the right side at given (α, θ) .

Instead, we test the validity of the diffusion approximation independent of the particle-surface kinetics by taking g_+ to be exactly 1. In the general case, the diffusion approximation for the density, $\rho_d(r,\alpha)$, is

$$\rho_d(r,\alpha) = 2\pi c_0 + \sum_{m=1}^{\infty} \left(a_m \frac{\cos m\alpha}{r^m} + b_m \frac{\sin m\alpha}{r^m} \right)$$
 (59)

$$\begin{bmatrix} a_m \\ b_m \end{bmatrix} = \frac{2}{\pi} \frac{R^{m+1}}{m} \int_{-\pi}^{\pi} J_{\mathbf{n}}(\alpha) \begin{bmatrix} \cos m\alpha \\ \sin m\alpha \end{bmatrix} d\alpha \tag{60}$$

where $J_{\rm n}(\alpha) \equiv \hat{n} \cdot \mathbf{J}(R,\alpha)$ is the normal flux at the boundary. Reference [65] works out a strategy for estimating $J_{\rm n}$ from g_+ . The idea is to treat the boundary as locally planar and use the machinery from section 5.3 to compute the solution close to the boundary (see appendix B). Figure 7 compares $J_{\rm n}(\alpha)$ calculated in this way for R=1 with the numerical solution from PDE2D. The agreement is surprisingly good considering that R is equal to the persistence length $\ell=1$, which a priori would call into question the accuracy of the locally planar approximation. For larger R, the approximation is even better [65]. In particular, we find the simple expression $J_{\rm n}(\alpha) \approx (R \cos \alpha)^{-1}$ to be accurate for $R \gg 1$, which in the multipole expansion for the density, equation (53), implies a dipole moment

$$\mathbf{p} = (a_1, b_1) = (4R, 0), \quad (R \gg 1). \tag{61}$$

Figure 7 compares the resulting ρ_d with the finite-element solution. If we exclude the region within a persistence length of the boundary (white annulus), the maximum percent deviation of ρ_d is about 5%. Thus, the diffusion approximation works very well in a nontrivial curvilinear geometry, where an exact solution by separation of variables is no longer possible.

7. Illustration 2: elliptic geometry

In the polar geometry, an asymmetry in the particle-surface interaction is required to generate long-range flow; otherwise, the net particle current is 0 everywhere and density decays exponentially away from the boundary. In particular, a purely repulsive spherical inclusion does not generate currents. In this section, we turn to an elliptic geometry, in which the requisite asymmetry is present in the shape of the boundary itself. Experimentally, such geometries would allow one to engineer long-range flows without having to tune particle-surface interactions.

7.1. Problem setup

Figure 8 shows the setup: we take our boundary to be a vertically oriented ellipse E with semimajor axis a, semiminor axis b, and foci at $(0, \pm c)$ where $c \equiv \sqrt{b^2 - a^2}$. We define elliptic coordinates (μ, η) ,

$$\begin{cases} x = c \sinh \mu \cos \eta & 0 \leqslant \mu < \infty \text{ and } 0 \leqslant \eta < 2\pi \\ y = c \cosh \mu \sin \eta \end{cases}$$
 (62)

such that E is defined by the constant- μ surface $\mu = \mu_0 \equiv \operatorname{arccosh}(b/c)$. The diffusion solution can be written in terms of μ and η using the general expression

$$f_d(\mathbf{r}, \theta) = c_0 + \beta(\mathbf{r}) - \epsilon^2 \nabla \beta(\mathbf{r}) \cdot \hat{u} + \frac{\epsilon^3}{4} (\nabla \nabla \beta(\mathbf{r}))_{ij} \hat{u}_i \hat{u}_j + \cdots$$
 (63)

where $\nabla^2 \beta(\mathbf{r}) = 0$. Conveniently, the Laplacian is just $\nabla^2 = \partial_{\mu}^2 + \partial_{\nu}^2$, so that $\beta(\mu, \eta)$ can be expanded as

$$\beta(\mu, \eta) = \sum_{m=1}^{\infty} e^{-m\mu} \left(a_m \cos m\eta + b_m \sin m\eta \right). \tag{64}$$

In the diffusion approximation, the boundary condition is

$$(\hat{e}_{\mu} \cdot \nabla \beta(\mu, \eta))|_{\mu = \mu_0} = -J_{\mathbf{n}}(\eta) \quad \to \quad \frac{1}{c(\sinh^2 \mu_0 + \cos^2 \eta)^{1/2}} \frac{\partial \beta}{\partial \mu} = -J_{\mathbf{n}}(\eta) \tag{65}$$

where \hat{e}_{μ} is the μ -coordinate vector (which is the same as the unit normal vector) and $J_{\rm n}(\eta)$ is the normal flux. Thus,

$$a_{m} = \frac{c}{m\pi} e^{m\mu_{0}} \int_{0}^{2\pi} \cos m\eta \left(\sinh^{2}\mu_{0} + \cos^{2}\eta\right)^{1/2} J_{n}(\eta) d\eta$$
 (66)

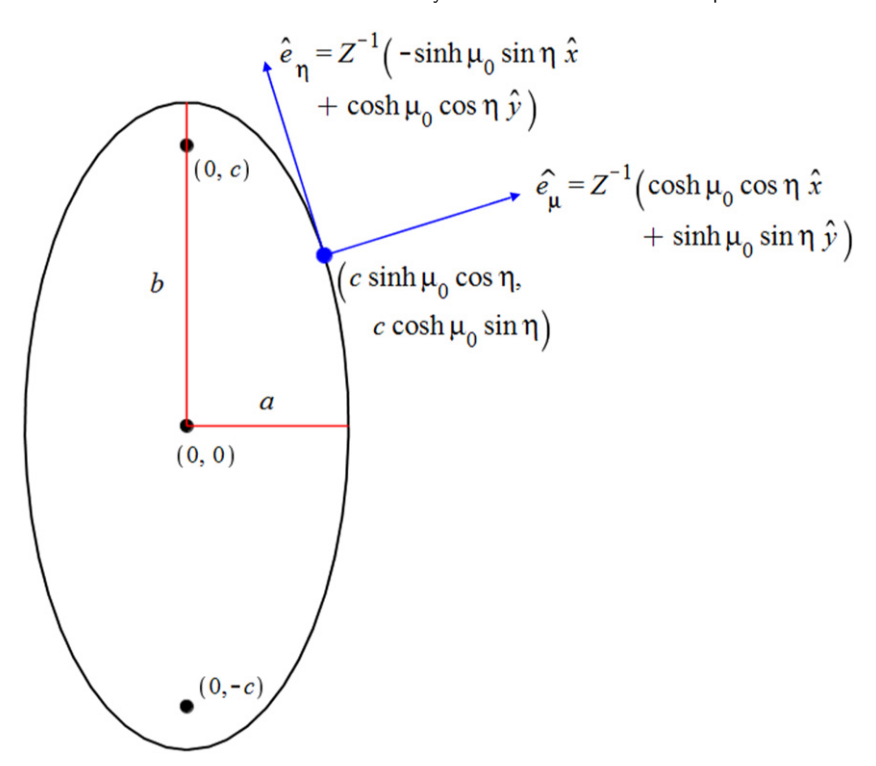


Figure 8. Elliptic geometry. We define elliptic coordinates (μ, η) by $x = c \sinh \mu \cos \eta$ and $y = c \cosh \mu \sin \eta$, where $c = \sqrt{b^2 - a^2}$. These are orthogonal coordinates, and the constant μ surfaces are confocal ellipses. In particular, $\mu = \mu_0 \equiv \operatorname{arccosh}(b/c)$ defines the ellipse depicted on the right. The blue arrows are the unit tangent and normal vectors at the point (μ_0, η) ; the unit normal vector is the same as the coordinate vector \hat{e}_{μ} , and similarly the tangent vector is \hat{e}_{η} . $Z^{-1} = (\cosh^2 \mu_0 \cos^2 \eta + \sinh^2 \mu_0 \sin^2 \eta)^{-1/2}$ is a normalization factor.

and similarly for b_m . Transforming from (μ, η) to (x, y) gives

$$\beta(\mu, \eta) = \frac{\mathbf{p} \cdot \hat{r}}{r} + \frac{Q_{ij}\hat{r}_i\hat{r}_j - (1/2)\operatorname{Tr}\mathbf{Q}}{r^2} + \mathcal{O}\left(\frac{1}{r^3}\right)$$
(67)

where

$$p = \frac{c}{2} (a_1, b_1); \qquad \mathbf{Q} = \frac{c^2}{4} \begin{pmatrix} a_2 & b_2 \\ b_2 & a_2 \end{pmatrix}.$$
 (68)

7.2. Test of the diffusion approximation

Figure 9 compares the diffusion solution with PDE2D for a=10, b=50, and the boundary condition

$$f(\mu_0, \eta, \theta) = \cos^2 \eta \tag{69}$$

$$\lim_{\mu \to \infty} f(\mu, \eta, \theta) = \text{constant.} \tag{70}$$

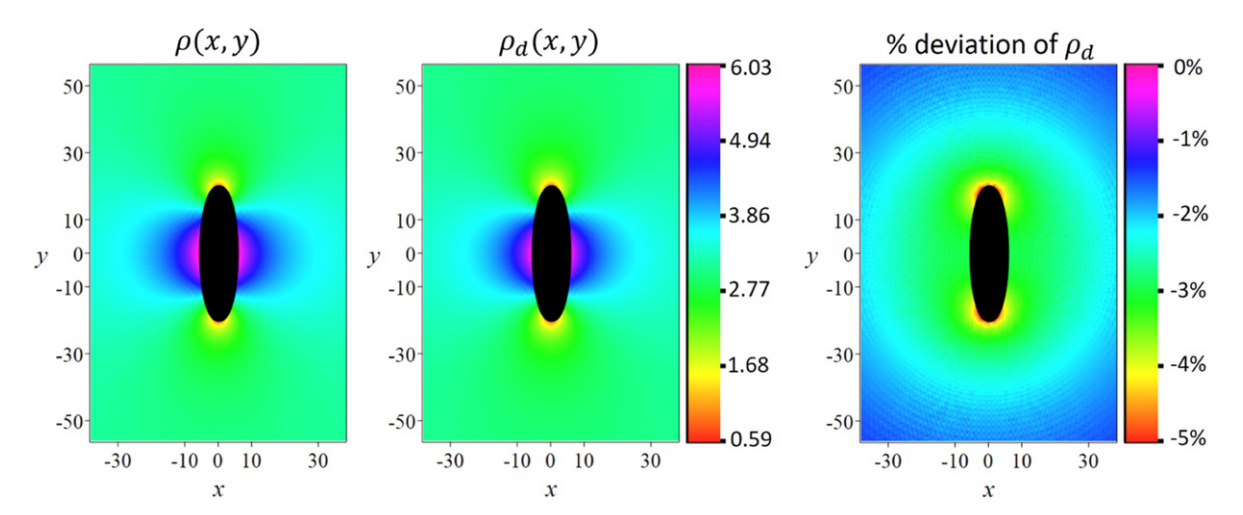


Figure 9. Density profiles corresponding to the boundary condition $f(\mu_0, \eta, \theta) = \cos^2 \eta$ and $f \to \text{constant}$ as $\mu \to \infty$. The $\mu = \mu_0$ coordinate surface defines an ellipse (black) with semimajor axis $b = 20\ell$ and semiminor axis $a = 5\ell$. The left and middle plots show the density from PDE2D and the diffusion approximation, respectively. The rightmost plot shows the percent deviation, which is systematic but small.

The agreement is on par with what we saw for the circular geometry. Of course, for a physical system the boundary conditions must be derived self-consistently from the underlying equations of motion, (1) and (2). To apply the diffusion approximation, in particular, we need to know the boundary normal flux. Here, we present a kinetic argument that approximates this quantity in the case of a long and thin ellipse (a/b small), and moderate to large persistence length ℓ .

The idea is that in these circumstances, a particle which adsorbs onto the surface tends to drive itself toward the ends of the ellipse before it significantly changes its orientation. This implies that most particles leave the surface in the vicinity of the points $(0, \pm b)$. By contrast, if ℓ were much smaller than b, then particles would have sufficient time to reorient themselves and leave before they travel too far from where they got adsorbed. To know the net flux, we also have to estimate the incoming flux of particles. Here, we simply take this to be constant along the surface: the idea is that a particle returning to the surface has spent enough time in the bulk to forget where it left the surface. Again, we expect this to be a reasonable approximation for sufficiently large ℓ .

From the above, we are led to the following expression for the boundary normal flux:

$$J_{n}(\eta) = \frac{\chi}{2a} \left[\delta \left(\eta - \frac{\pi}{2} \right) + \delta \left(\eta - \frac{3\pi}{2} \right) - \frac{2a}{c I_{0}} \right]$$
where $I_{0} \equiv \int_{0}^{2\pi} \left(\sinh^{2} \mu_{0} + \cos^{2} \eta \right)^{1/2} d\eta$. (71)

The δ -functions model the outgoing flux due to particles leaving near $(0, \pm b)$, and the constant offset $(1/\pi)$ accounts for the incoming flux, its value chosen so that the net flux

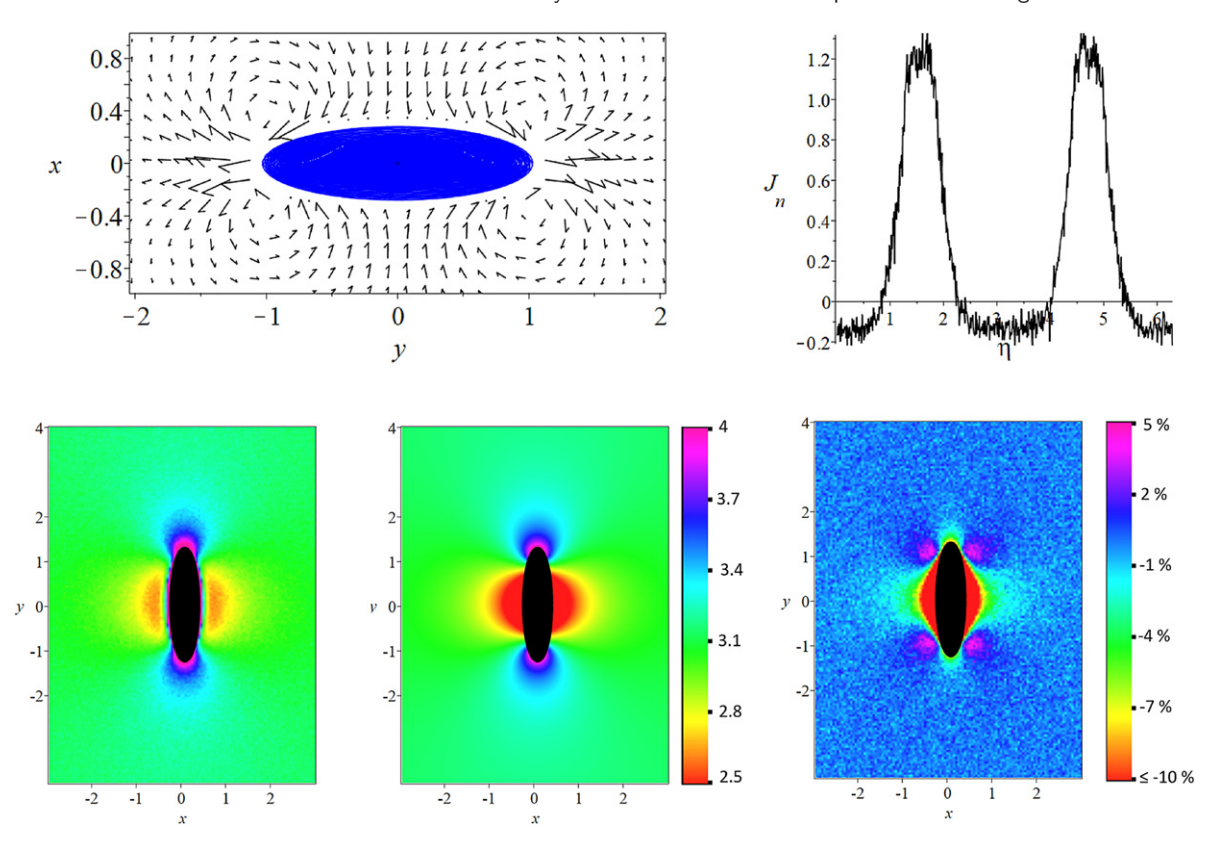


Figure 10. Flux field and density for a bath of ABPs in contact with a fixed, purely repulsive ellipse with semimajor axis $b = \ell$ and semiminor axis $a = 0.25\ell$. The radius of an ABP is 0.1ℓ . The top two plots show the flux field and normal flux $J_{\rm n}$ obtained from simulation of the particle dynamics (1) and (2). The bottom left plot shows the density field from simulations. The bottom middle plot shows the diffusion approximation using the boundary condition (71). The agreement is fairly good considering the simplifications leading up to (71).

integrated along the surface is 0. The function $F(\eta)$ expresses these two contributions up to an undetermined constant χ , which has units of inverse time. Physically, χ quantifies the number of particles impinging on (or leaving) the surface in unit time. With this interpretation, a rough guess is that $\chi \approx 2c_0 \mathcal{A} v_0$, v_0 being the self-propulsion velocity, c_0 the (constant) value of f at infinity, and \mathcal{A} the surface area.

Figure 10 compares this prediction with simulation for $a = 0.25\ell$, $b = \ell$, and particle radius 0.1ℓ . The measured normal flux reflects the general shape of $F(\eta)$, showing peaks near $\cos \eta = 0$ and a constant offset. The predicted density ρ_d using equation (71) also compares well with the simulation: most of the error is concentrated in the near field, particularly around $(\pm a, 0)$. In the multipole expansion for the density (equation (67)), the predicted dipole moment is 0, and the quadrupole moment is $Q_{12} = Q_{21} = 0$,

$$Q_{11} = Q_{22} = -\frac{\mathcal{A}}{8\pi} (a+b)^2 \left(1 + \frac{I_2}{I_0}\right)$$
 (72)

$$I_m \equiv \int_0^{2\pi} \cos m\eta \left(\sinh^2 \mu_0 + \cos^2 \eta\right)^{1/2} d\eta. \tag{73}$$

In the limit $b \gg a$, this becomes $Q_{11} = Q_{22} \approx (2\pi)^{-1}(a+b)^2 \mathcal{A}$. For the problem in figure 10, the numerical value is $Q_{11} \simeq -0.42$.

A caveat is that the predicted flux, equation (71), is larger than the measured flux by roughly an order of magnitude. Despite this discrepancy, using (71) as the boundary condition on the diffusion solution ends up giving a more accurate prediction than using the measured flux. A likely explanation is that the fraction of the flux contained in the exact diffusion solution is greater than 1, the excess being balanced by the boundary layer piece of the solution. Then, the better agreement of (71) is due to a cancellation of two errors: the first overestimating the flux and the second underestimating the fraction of flux contained in the diffusion solution. Such situations are expected to occur when ℓ is the same order of magnitude as the length scale of the boundary conditions, as is the case here. Nevertheless, our results suggest that the diffusion approximation may give a qualitative understanding of the steady state even in these cases.

8. Summary

Our goal has been to develop an analytical framework to understand ABP steady states in the presence of boundaries. A key simplification that enables this effort is the diffusion approximation, equation (17), which says that the asymptotic ('diffusion') solution of (4) carries all the particle flux. Our results from sections 5–7 demonstrate the validity of this approximation when variations of the boundary data are small compared with the persistence length ℓ (which we set to 1 in the majority of our analysis). More generally, the diffusion approximation provides a map between violations of detailed balance at the boundary and corresponding mass fluxes in the bulk. This mapping could be a useful design principle for nonequilibrium steady states in general: by tuning particle-boundary interactions or boundary geometry, one could achieve the desired properties of the bulk steady state.

In future work, the extension of our framework to higher-dimensional problems could be useful, as a way to mitigate the exponential increase in computational burden of a direct numerical simulation. Even in cases where higher accuracy is desired than provided by the diffusion approximation, the general form of the asymptotic solution could be used to accelerate numerical algorithms [70]. Along these lines, a study of long-range flow fields in 3D ABP systems would be interesting.

Similarly, the extension to time-dependent problems would be interesting. The characteristics of the long-time approach to diffusion have lately been considered in the active matter context [28, 71–74], and an asymptotic approach such as ours could provide additional insight. For the ABPs, a possible starting point is to scale equation (4) as

$$\epsilon^2 \partial_t f + \epsilon \left(\cos \theta \, \partial_x f + \sin \theta \, \partial_y f\right) = \partial_\theta^2 f \tag{74}$$

where ϵ is a formal perturbation parameter. Then, substituting $f \sim f_0 + \epsilon f_1 + \cdots$ gives $f = \text{const.} + \beta(x, y, t) + \mathcal{O}(\epsilon)$, where β solves $\partial_t \beta = (1/4)\nabla^2 \beta$. Thus, in this scaling, the long-time evolution is indeed diffusive. Since the initial value problem does not involve a complicated half-range analysis, connecting the diffusion solution with initial conditions should pose fewer technical difficulties than the analogous boundary value problem (for e.g. see [75, 76]). Thus, our work, while directly providing an analytical handle on ABP steady states, can serve as a springboard to apply similar tools to other problems in active matter.

While preparing this article, we learned of a preprint [77] that also treats bulk-boundary correspondence and long-range effects in active colloid steady states, and arrives at similar conclusions regarding the density and current profiles near a planar wall. Their treatment of interparticle interactions is an interesting and nontrivial extension to our analysis, which is restricted to dilute systems. On the other hand, our work goes beyond theirs in that we calculate exactly the boundary layer in the planar problem, as well as treat more general curvilinear geometries. Moreover, by formulating the microscopic transport equation as a boundary value problem, we provide a systematic procedure for constructing and validating bulk-boundary correspondence principles such as the diffusion approximation in section 4.

Acknowledgments

We acknowledge support from the Brandeis Center for Bioinspired Soft Materials, an NSF MRSEC, DMR-1420382 (C G W, A B, M F H), NSF-MRSEC-2011486 (A B, M F H), NSF DMR-1149266 and BSF-2014279 (C G W and A B), and DMR-1855914 (M F H). C G W also acknowledges support from the Heising-Simons Foundation, the Simons Foundation, and National Science Foundation Grant No. NSF PHY-1748958. Computational resources were provided by the NSF through XSEDE computing resources (MCB090163) and the Brandeis HPCC which is partially supported by the Brandeis MRSEC and NSF OAC-1920147. We also thank Granville Sewell for assistance with PDE2D.

Appendix A. Numerical methods

For the particle-based simulations, we numerically integrate (1) and (2) using a stochastic Euler algorithm. Our simulations are ideal for GPU architectures since the code is trivial to parallelize (particles are non-interacting), and so we wrote a CUDA implementation alongside C++ code for CPUs. In most cases, we use timestep $\Delta t = \mathcal{O}(10^{-5}D_r^{-1})$. In the C++ code, however, we use $10\Delta t$ as timestep far from the boundary, where the solution is slowly varying, which results in a substantial speed-up. We take statistics at intervals of D_r^{-1} , beginning at a threshold time of around $10^4D_r^{-1}$. All simulations use $D_t = 0.001\ell^2D_r$, except for the ellipse problem from section 7, where we use $D_t = 0.0001\ell^2D_r$. The reason for a smaller value is to ensure the width δ of the diffusive boundary layer scales appropriately with the dimensions of the ellipse.

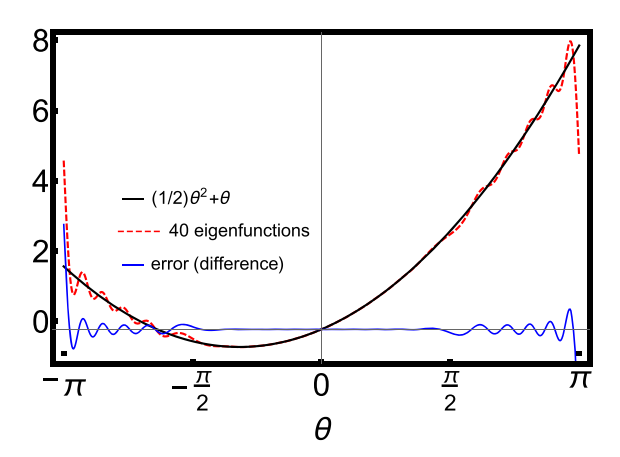


Figure 11. Test of the full-range completeness conjecture for $\mu = 1$. Using a least-squares technique, we approximate the function $(1/2)\theta^2 + \theta$ (black) as a linear combination of the first 40 eigenfunctions (red dashed). The blue curve shows the difference between the two.

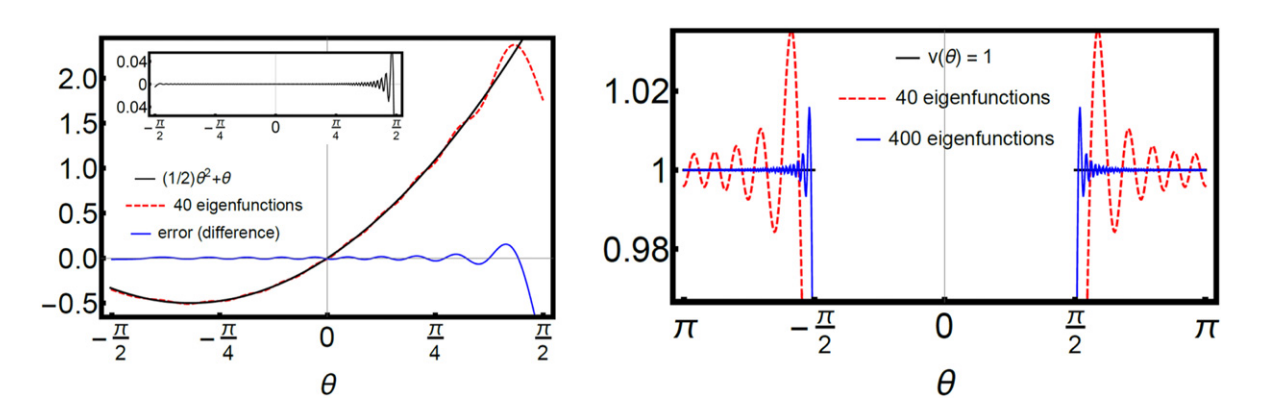


Figure 12. Test of the half-range completeness conjecture for $\mu=1$. In the left panel, we test the conjecture on the positive half range, $\cos\theta>0$. Using a least-squares technique, we approximate the function $(1/2)\theta^2+\theta$ (black) as a linear combination of the first 40 eigenfunctions (red dashed). The blue curve shows the difference using 40 eigenfunctions, and the inset shows the difference using 400 eigenfunctions. Similarly, in the right panel, we test the conjecture on the negative half range, $\cos\theta<0$, where the function $v(\theta)=1$ is expanded using 40 and 400 eigenfunctions, respectively.

For the circular geometry (section 6.4), we use the particle-surface interaction potential

$$V(r,\alpha) = \frac{\tanh(100R - 100r) + 1}{10} \left[\tanh\left(5\alpha - \frac{5\pi}{2}\right) + \tanh\left(\frac{15\pi}{2} - 5\alpha\right) - 2 \right] + \frac{1}{10} \left(r + \frac{1}{19(r - R + 1)^{19}}\right) - \frac{191}{190} \left[1 - H(R - r)\right]$$
(A1)

which is continuous in the region of interest. Here, H(z) is the Heaviside function. Roughly speaking, the potential gives rise to a 'ratchet' along the surface of the circle, where x < 0 particles experience a strong but short-ranged force in the direction of $-\hat{r}$. By contrast, fixing r and varying α from the left hemisphere to the right, particles experience a weaker but longer-range force in the direction of $-\hat{\alpha}$, i.e. pointing towards the left hemisphere. The asymmetry between the radial and angular components forms a ratchet that rectifies the motion of the ABPs in agreement with previous work on self-propelled particles in ratchet potentials [50]. The net effect is that particles tend to be bound on the left side of the sphere and released on the right.

The interactions for the elliptic geometry are defined as follows. For the repulsive force, $\hat{e}_{\eta} \cdot \mathbf{F}_{r} = 0$ and

$$\frac{\hat{e}_{\mu} \cdot \mathbf{F}_r}{\ell D_r} = \begin{cases} (10s)^{-40} - 1 & 0 < s \le 0.1\\ 0 & s > 0.1 \end{cases}$$
(A2)

where s is the distance from an ellipse with semiminor and semimajor axes a and b. While we would like to identify effective semimajor and semiminor axes induced by \mathbf{F}_r , these are not well-defined because the constant-distance surfaces, along which $\hat{e}_{\mu} \cdot \mathbf{F}_r$ is constant, are not ellipses. However, since the range of the force is small compared with the major- and minor-axes, this discrepancy is small. Indeed, a numerical calculation shows that effective values $a_{\text{eff}} = a + 0.1\ell$ and $b_{\text{eff}} = b + 0.1\ell$ define an ellipse that very nearly coincides with the $s = \ell$ surface.

We use the Fortran-based software PDE2D (www.pde2d.com) for our finite element computations. For solving three-dimensional problems like (4), it uses a collocation method with tricubic Hermite basis functions [78, 79]. In our analysis, we use 20 gridlines in the θ variable, 50 in the angular coordinate α or η , and at least 90 in the radial coordinate r or μ .

Appendix B. Supplementary material for the 2D planar problem

B.1. Completeness conjectures

To test the full-range completeness conjecture, we expand a function $v(\theta)$ in the subspace consisting of the first 2(N+1) eigenfunctions, for some N:

$$v(\theta) = a_0^+ \Omega_0^+ + a_0^- \Omega_0^- + \sum_{|k| \leqslant N, k \neq 0} a_k \Omega_k$$
(B1)

where the Ω_k have arguments $(\theta, |\mu|)$. To determine the coefficients a_k , we minimize the squared difference

$$\int_{-\pi}^{\pi} \left[v(\theta) - a_0^+ \Omega_0^+ - a_0^- \Omega_0^- - \sum_{|k| \leqslant N, k \neq 0} a_k \Omega_k \right]^2 |\cos \theta| \, \mathrm{d}\theta.$$
 (B2)

The minimization can be done efficiently on a computer since it only involves the solution of a $2(N+1) \times 2(N+1)$ linear system. The half-range conjectures are tested similarly.

For the positive-range conjecture, we minimize

$$\int_{\cos \theta > 0} \left[v(\theta) - a_0^+ \Omega_0^+ - \sum_{0 < k \le N} a_k \Omega_k \right]^2 |\cos \theta| \, \mathrm{d}\theta \tag{B3}$$

and similarly for the negative-range.

Representative tests are shown in figures 11 and 12—specifically, taking $v(\theta) = (1/2)\theta^2 + \theta$ on the full range and positive half range, and $v(\theta) = 1$ on the negative half range. All three cases provide good support for the corresponding completeness conjectures.

B.2. Boundary value problem

Solving the full boundary value problem requires matching the coefficients in the general solution (40) to the boundary data. Specifically, if

$$f(0, y, \theta) = g(y, \theta) = \int_0^\infty d\mu \, q(\mu, \theta) \cos \mu y + \int_0^\infty d\mu \, p(\mu, \theta) \sin \mu y, \quad \cos \theta > 0$$
 (B4)

then, for given μ , we must find real constants a_k, b_k, c_k, d_k such that

$$\sum_{k\geqslant 0} (+a_k \Omega_k - b_k \Upsilon_k + c_k \Omega_k + d_k \Upsilon_k) = q(\mu, \theta) \quad \text{where cos } \theta > 0$$
 (B5)

$$\sum_{k\geq 0} (+a_k \Omega_k + b_k \Upsilon_k + c_k \Omega_k - d_k \Upsilon_k) = p(\mu, \theta) \quad \text{where cos } \theta > 0$$
 (B6)

$$\sum_{k\geqslant 0} \left(+a_k \Omega_k + b_k \Upsilon_k - c_k \Omega_k + d_k \Upsilon_k \right) = 0 \tag{B7}$$

$$\sum_{k\geq 0} \left(-a_k \Omega_k + b_k \Upsilon_k + c_k \Omega_k + d_k \Upsilon_k \right) = 0 \tag{B8}$$

where the Ω_k and Υ_k have arguments θ , $|\mu|$. To solve these equations, we assume the halfrange completeness conjecture on the Ω_k . Then, we require that the difference between the lhs and rhs of each equation is orthogonal to each of the Ω_j with respect to inner product $\langle f,g\rangle = \int_{\cos\theta>0} fg\cos\theta \,\mathrm{d}\theta$. In practice, we choose some upper cutoff k=N. Then, we obtain the $4N\times 4N$ linear system

$$\begin{pmatrix} A & -B & A & B \\ B & A & B & -A \\ B & A & -B & A \\ -A & B & A & B \end{pmatrix} \begin{pmatrix} \mathbf{a} \\ \mathbf{b} \\ \mathbf{c} \\ \mathbf{d} \end{pmatrix} = \begin{pmatrix} \mathbf{u} \\ \mathbf{v} \\ 0 \\ 0 \end{pmatrix}$$
(B9)

where $\mathbf{a}, \mathbf{b}, \mathbf{c}, \mathbf{d}$ are N-dimensional vectors whose components are the coefficients $a_k, b_k, c_k, d_k, k \leq N$; and

$$A_{ij} = \langle \Omega_i, \Omega_j \rangle; \qquad B_{ij} = \langle \Omega_i, \Upsilon_j \rangle$$
 (B10)

$$\mathbf{u}_i = \langle q, \Omega_i \rangle; \qquad \mathbf{v}_i = \langle p, \Omega_i \rangle.$$
 (B11)

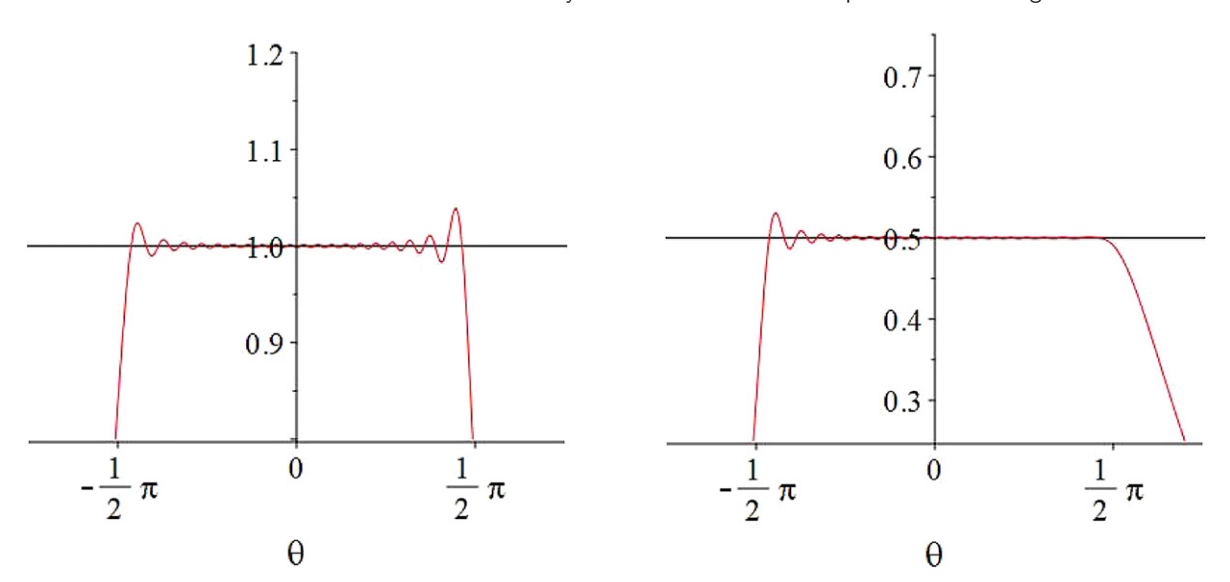


Figure 13. Here we test the numerical procedure for calculating the expansion coefficients a_k, b_k, c_k, d_k in equation (B8) (compared with equation (40)). We use $\mu = 1$, $q(\theta) = 1$, and $p(\theta) = 1/2$. The left plot shows the lhs of equation (B5) using the calculated a_k, b_k, c_k, d_k and an upper cutoff k = 40, and similarly the right plot shows the lhs of (B6). We found the lhs of (B7) and (B8) to be 0 within machine precision.

We have found N=40 to be sufficient in most cases, although we have tested up to N=400 in some calculations. Figure 13 shows an example with $\mu=2$, $q(\theta)=1$, $p(\theta)=1/2$, and N=40.

Appendix C. Locally planar approximation

Here, we illustrate the type of 'locally planar' approximation that can be used to estimate the boundary normal flux. We use the same setup as from section 6.4, that is, a circular geometry with boundary data

$$f(R, \alpha, \theta) = \begin{cases} 1 & \text{where } \cos \alpha > 0 & \text{and} & \cos(\theta - \alpha) > 0 \\ 0 & \text{where } \cos \alpha < 0 & \text{and} & \cos(\theta - \alpha) > 0 \end{cases}$$
 where cos $\alpha < 0$ and cos $(\theta - \alpha) > 0$ (C1) unspecified else

$$\lim_{r \to \infty} f(r, \alpha, \theta) = c_0 = \text{constant}$$
 (C2)

to be solved on $R < r < \infty$, $0 < \alpha < 2\pi$, $-\pi < \theta < \pi$. The constant c_0 is constrained by the boundary condition at r = R. In a planar problem, c_0 would correspond to the constant Fourier mode of (C1), which in the present case gives $c_0 = 1/2$. For the range of R-values considered here, the actual value is slightly smaller and carries a weak R-dependence. For instance, $c_0 \approx 0.466$ for R = 1 and 0.452 for R = 5. However, consistent with the level of approximation adopted elsewhere in this section, we simply take

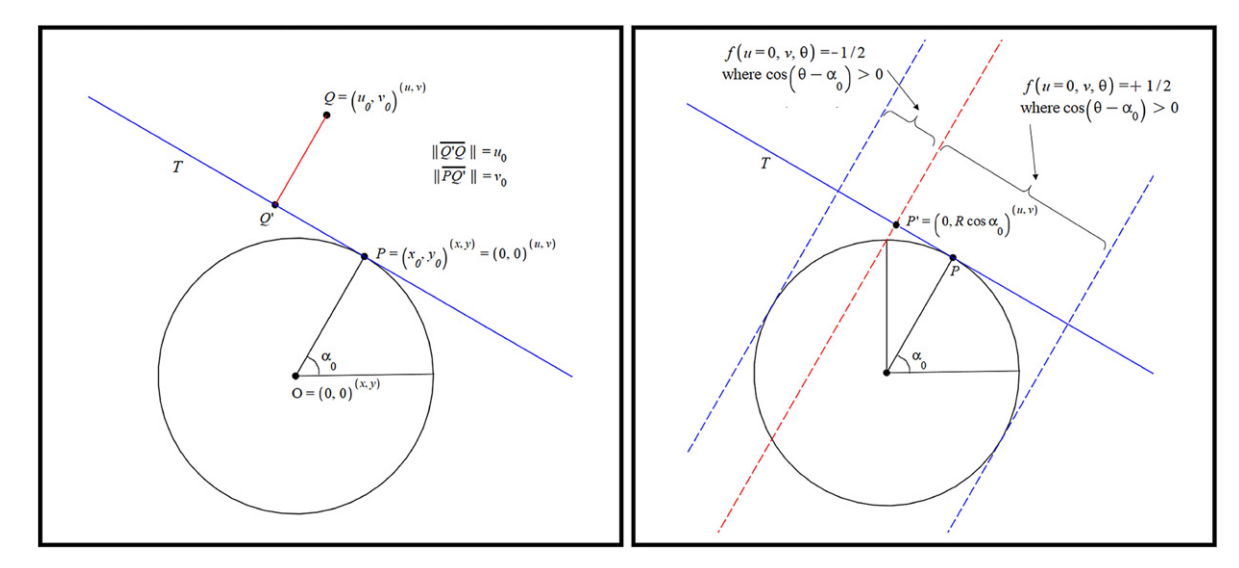


Figure 14. Ingredients in the locally planar approximation. The left panel illustrates the (u, v) coordinate system corresponding to a point P on the boundary. As discussed in appendix \mathbb{C} , u and v are the horizontal and vertical coordinates in a planar half-space problem bounded on the left by the tangent line T (u = 0). The right panel shows how we approximate the boundary conditions at u = 0 by projecting onto T the boundary conditions ($\mathbb{C}5$), which sit on the surface of the sphere. The idea is that particles retain their approximate angular distribution as they leave the sphere and pass through T.

 $c_0 = 1/2$. Then, it is convenient to subtract c_0 from the overall solution and solve the transformed problem

$$f(R, \alpha, \theta) = \begin{cases} +1/2 & \text{where } \cos \alpha > 0 & \text{and} & \cos(\theta - \alpha) > 0 \\ -1/2 & \text{where } \cos \alpha < 0 & \text{and} & \cos(\theta - \alpha) > 0 \end{cases}$$
(C3)
$$\lim_{r \to \infty} f(r, \alpha, \theta) = 0.$$
 (C4)

The locally planar approximation is illustrated in figure 14. Consider a point P on the boundary, with Cartesian coordinates (x_0, y_0) and polar coordinates (R, α_0) , and tangent line T. We can define an infinite half-space problem if we consider T as defining a planar boundary: if $f(r, \alpha, \theta)$ is known along the entirety of T, then we can use the methods of section 5 to solve for $f(r, \alpha, \theta)$ on the infinite half space outside of T (on the side opposite the circle).

Towards this end, for a point Q above T, let u be the perpendicular distance from T and v be the parallel distance from P. We denote these coordinates with superscript (u, v) such that $Q = (u, v)^{(u,v)}$ and $P = (0, 0)^{(u,v)}$. In terms of these coordinates, suppose we know $f(u = 0, v, \theta)$ on $-\infty < v < \infty$ and where $\cos(\theta - \alpha_0) > 0$. Then, $f(u, v, \theta)$ solves an infinite half-space problem on u > 0 of the type solved analytically

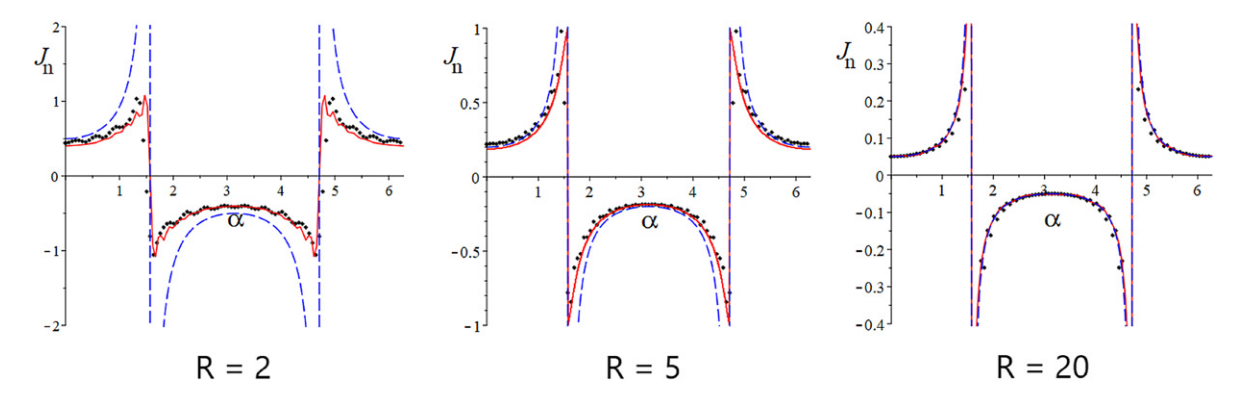


Figure 15. Some tests of the locally planar approximation for R = 2, 5, 20. The black diamonds show the normal flux $J_n(\alpha)$ evaluated numerically using PDE2D. The solid red curve shows the locally planar approximation described in appendix C, and the blue dashed curve shows the function $(R \cos \alpha)^{-1}$. The accuracy of the approximations increases with R, but is good even for R = 2.

in section 5, with boundary conditions $f(u = 0, v, \theta) = g(v, \theta)$ defined on $-\infty < v < \infty$, $\cos(\theta - \alpha_0) > 0$. It remains to determine $g(v, \theta)$.

Suppose we can satisfy ourselves with solving for f only very close to P. This is certainly true if our goal is to determine the boundary normal flux at P. Being close to P means that the form of $g(u,\theta)$ for large |v| influences the solution much less than its behavior near v=0, so we can get away with some approximations in the former region. In this spirit, the locally planar approximation projects the boundary conditions at r=R onto T. For the point P, for instance, we would take

$$g(v,\theta)|_{\cos(\theta-\alpha_0)>0} = \begin{cases} +1/2 & -R < u < R \cos \alpha_0 \\ -1/2 & R \cos \alpha_0 < u < R \\ 0 & |u| > R \end{cases}$$
 (C5)

$$\lim_{r \to \infty} f(r, \alpha, \theta) = a_0 = \text{constant.}$$
 (C6)

Though less accurate for large |v|, this approximation will generate accurate boundary conditions near P, and the exact boundary condition at P itself. Thus, the resulting solution $f(r, \alpha, \theta)$ is also expected to be accurate near P.

Figure 15 tests the approximation for several R, comparing the calculated boundary normal flux $J_{\rm n}(R,\alpha)$ with the finite-element solution. The agreement is surprisingly good over a range of R values. If R is large and $\cos \alpha$ not too close to 0, then $J_{\rm n}(R,\alpha)$ is $J_{\rm n}(R,\alpha) \approx (R \cos \alpha)^{-1}$, which is also shown in figure 15.

References

- [1] Ramaswamy S 2010 Annu. Rev. Condens. Matter Phys. 1 323
- [2] Marchetti M C, Joanny J F, Ramaswamy S, Liverpool T B, Prost J, Rao M and Simha R A 2013 Rev. Mod. Phys. 85 1143
- [3] Bechinger C, Di Leonardo R, Löwen H, Reichhardt C, Volpe G and Volpe G 2016 Rev. Mod. Phys. 88 045006
- [4] Zöttl A and Stark H 2016 J. Phys.: Condens. Matter 28 253001
- [5] Yoshinaga N 2017 J. Phys. Soc. Japan 86 101009
- [6] Ramaswamy S 2017 J. Stat. Mech. 054002
- [7] Needleman D and Dogic Z 2017 Nat. Rev. Mater. 2 17048
- [8] Saintillan D 2018 Annu. Rev. Fluid Mech. 50 563
- [9] Fodor É and Cristina Marchetti M 2018 Physica A 504 106
- [10] Seifert U 2019 Annu. Rev. Condens. Matter Phys. 10 171
- [11] Sanchez T, Chen D T N, DeCamp S J, Heymann M and Dogic Z 2012 Nature 491 431
- [12] Dombrowski C, Cisneros L, Chatkaew S, Goldstein R E and Kessler J O 2004 Phys. Rev. Lett. 93 098103
- [13] Kaiser A, Peshkov A, Sokolov A, ten Hagen B, Löwen H and Aranson I S 2014 Phys. Rev. Lett. 112 158101
- [14] Deseigne J, Léonard S, Dauchot O and Chaté H 2012 Soft Matter 8 5629
- [15] Bricard A, Caussin J-B, Desreumaux N, Dauchot O and Bartolo D 2013 Nature 503 95
- [16] Palacci J, Sacanna S, Steinberg A P, Pine D J and Chaikin P M 2013 Science 339 936
- [17] van der Vaart K, Sinhuber M, Reynolds A M and Ouellette N T 2019 Sci. Adv. 5 eaaw9305
- [18] Cepelewicz J 2019 How swarming insects act like fluids Quanta Magazine
- [19] Tennenbaum M, Liu Z, Hu D and Fernandez-Nieves A 2015 Nat. Mater. 15 54
- [20] Becco C, Vandewalle N, Delcourt J and Poncin P 2006 Physica A 367 487
- [21] Cambuí D S and Rosas A 2012 Physica A **391** 3908
- [22] Attanasi A et al 2014 Nat. Phys. 10 691
- [23] Narayan V, Menon N and Ramaswamy S 2006 J. Stat. Mech. P01005
- [24] Narayan V, Ramaswamy S and Menon N 2007 Science 317 105
- [25] Walsh L and Menon N 2016 J. Stat. Mech. 083302
- [26] Junot G, Briand G, Ledesma-Alonso R and Dauchot O 2017 Phys. Rev. Lett. 119 028002
- [27] Walsh L, Wagner C G, Schlossberg S, Olson C, Baskaran A and Menon N 2017 Soft Matter 13 8964
- [28] Scholz C, Jahanshahi S, Ldov A and Löwen H 2018 Nat. Commun. 9 5156
- [29] Savoie W, Cannon S, Daymude J J, Warkentin R, Li S, Richa A W, Randall D and Goldman D I 2018 Artif. Life Robot. 23 459
- [30] Hartnett K 2018 Smart swarms seek new ways to cooperate Quanta Magazine
- [31] Deblais A, Barois T, Guerin T, Delville P H, Vaudaine R, Lintuvuori J S, Boudet J F, Baret J C and Kellay H 2018 Phys. Rev. Lett. 120 188002
- [32] Dauchot O and Démery V 2019 Phys. Rev. Lett. 122 068002
- [33] Solon A P, Fily Y, Baskaran A, Cates M E, Kafri Y, Kardar M and Tailleur J 2015 Nat. Phys. 11 673
- [34] Wagner C G, Hagan M F and Baskaran A 2017 J. Stat. Mech. 043203
- [35] Wensink H H and Löwen H 2008 Phys. Rev. E **78** 031409
- [36] Volpe G, Buttinoni I, Vogt D, Kümmerer H-J and Bechinger C 2011 Soft Matter 7 8810
- [37] Elgeti J and Gompper G 2013 Europhys. Lett. 101 48003
- [38] Lee C F 2013 New J. Phys. **15** 055007
- [39] Ezhilan B, Alonso-Matilla R and Saintillan D 2015 J. Fluid Mech. 781 R4
- [40] Fily Y and Marchetti M C 2012 Phys. Rev. Lett. 108 235702
- [41] Redner G S, Hagan M F and Baskaran A 2013 Phys. Rev. Lett. 110 055701
- [42] Stenhammar J, Tiribocchi A, Allen R J, Marenduzzo D and Cates M E 2013 Phys. Rev. Lett. 111 145702
- [43] Stenhammar J, Marenduzzo D, Allen R J and Cates M E 2014 Soft Matter 10 1489
- [44] Wysocki A, Winkler R G and Gompper G 2014 Europhys. Lett. 105 48004
- [45] Cates M E and Tailleur J 2015 Annu. Rev. Condens. Matter Phys. 6 219
- [46] Stenhammar J, Wittkowski R, Marenduzzo D and Cates M E 2015 Phys. Rev. Lett. 114 018301
- [47] Ni R, Cohen Stuart M A, Dijkstra M and Bolhuis P G 2014 Soft Matter 10 6609
- [48] Redner G S, Wagner C G, Baskaran A and Hagan M F 2016 Phys. Rev. Lett. 117 148002
- [49] Wan M B, Olson Reichhardt C J, Nussinov Z and Reichhardt C 2008 Phys. Rev. Lett. 101 018102
- [50] Reichhardt C J O and Reichhardt C 2017 Annu. Rev. Condens. Matter Phys. 8 51
- [51] Baek Y, Solon A P, Xu X, Nikola N and Kafri Y 2018 Phys. Rev. Lett. 120 058002
- [52] Angelani L, Maggi C, Bernardini M L, Rizzo A and Di Leonardo R 2011 Phys. Rev. Lett. 107 138302

- [53] Ray D, Reichhardt C and Reichhardt C J O 2014 Phys. Rev. E $\bf 90$ 013019
- [54] Harder J, Mallory S A, Tung C, Valeriani C and Cacciuto A 2014 J. Chem. Phys. 141 194901
- [55] Ni R, Cohen Stuart M A and Bolhuis P G 2015 Phys. Rev. Lett. 114 018302
- [56] Leite L R, Lucena D, Potiguar F Q and Ferreira W P 2016 Phys. Rev. E 94 062602
- [57] Yamchi M Z and Naji A 2017 J. Chem. Phys. 147 194901
- [58] Li K, Guo F, Zhou X, Wang X, He L and Zhang L 2020 Sci. Rep. 10 11702
- [59] Zarif M and Naji A 2020 Phys. Rev. E **102** 032613
- [60] Torrik A, Naji A and Zarif M 2021 arXiv:2107.14464
- [61] Greenberg W, van der Mee C and Protopopescu V 1987 Boundary Value Problems in Abstract Kinetic Theory (Basel: Birkhauser)
- [62] Wagner C G and Beals R 2019 J. Phys. A: Math. Theor. 52 115204
- [63] Beals R and Protopopescu V 1987 J. Math. Anal. Appl. 121 370
- [64] Cercignani C 1990 Mathematical Methods in Kinetic Theory (Boston, MA: Springer)
- [65] Wagner C G 2020 Mathematics of nonequilibrium steady states in dilute active matter PhD Thesis
- [66] Chapman S and Cowling T 1970 The Mathematical Theory of Non-Uniform Gases 3rd edn (Cambridge: Cambridge University Press)
- [67] Grad H 1986 Thermodynamik Der Gase/Thermodynamics of Gases ed S Fluegge (Berlin: Springer) pp 205–94
- [68] Fisch N J and Kruskal M D 1980 J. Math. Phys. 21 740
- [69] Beals R 1985 J. Differ. Equ. **56** 391
- [70] Jin S 1999 SIAM J. Sci. Comput. 21 441
- [71] Sevilla F J and Sandoval M 2015 Phys. Rev. E $\bf 91$ 052150
- [72] Malakar K, Jemseena V, Kundu A, Vijay Kumar K, Sabhapandit S, Majumdar S N, Redner S and Dhar A 2018 J. Stat. Mech. 043215
- [73] Basu U, Majumdar S N, Rosso A and Schehr G 2019 Phys. Rev. E 100 062116
- [74] Villa-Torrealba A, Chávez-Raby C, de Castro P and Soto R 2020 Phys. Rev. E 101 062607
- [75] Malvagi F and Pomraning G C 1991 J. Math. Phys. 32 805
- [76] Grad H 1963 Phys. Fluids 6 147
- [77] Dor Y B, Ro S, Kafri Y, Kardar M and Tailleur J 2021 arXiv:2108.13409
- [78] Sewell G 2010 Adv. Eng. Softw. 41 748
- [79] Sewell G 2018 Solving Partial Differential Equation Applications with PDE2D (New York: Wiley)